

Fast, Safe, and Propellant-Efficient Spacecraft Planning under Clohessy-Wiltshire-Hill Dynamics

Joseph A. Starek,^a Edward Schmerling,^b and Gabriel D. Maher^b
Stanford University, Stanford, CA, 94305

Brent W. Barbee^c
NASA Goddard Space Flight Center, Greenbelt, MD, 20771

Marco Pavone^d
Stanford University, Stanford, CA, 94305

This paper presents a sampling-based motion planning algorithm for real-time and propellant-optimized autonomous spacecraft trajectory generation in near-circular orbits. Specifically, this paper leverages recent algorithmic advances in the field of robot motion planning to the problem of impulsively-actuated, propellant-optimized rendezvous and proximity operations under the Clohessy-Wiltshire-Hill (CWH) dynamics model. The approach calls upon a modified version of the Fast Marching Tree (FMT*) algorithm to grow a set of feasible trajectories over a deterministic, low-dispersion set of sample points covering the free state space. To enforce safety, the tree is only grown over the subset of *actively-safe samples*, from which there exists a feasible one-burn collision avoidance maneuver that can safely circularize the spacecraft orbit along its coasting arc under a given set of potential thruster failures. Key features of the proposed algorithm include: (i) theoretical guarantees in terms of trajectory safety and performance, (ii) amenability to real-time implementation, and (iii) generality, in the sense that a large class of constraints can be handled directly. As a result, the proposed algorithm offers the potential for widespread application, ranging from on-orbit satellite servicing to orbital debris removal and autonomous inspection missions.

^a Graduate Student, Aeronautics & Astronautics, 496 Lomita Mall, Rm 009, Stanford, CA, 94305

^b Graduate Student, Inst. for Computational and Mathematical Engineering, 475 Via Ortega, Stanford, CA, 94305

^c Aerospace Engineer, Navigation and Mission Design Branch (Mail Code 595), 8800 Greenbelt Rd, Greenbelt, MD, 20771, AIAA Senior Member

^d Assistant Professor, Aeronautics & Astronautics, 496 Lomita Mall, Rm 261, Stanford, CA, 94305, AIAA Member

I Introduction

Real-time autonomy for spacecraft proximity operations near circular orbits is an inherently challenging task, particularly for onboard implementation where computational capabilities are limited. Many effective real-time solutions have been developed for the *unconstrained* case (*e.g.*, state transition matrix manipulation [1], glideslope methods [2], safety ellipses [3, 4], and others [5]). However, the difficulty of real-time processing increases when there is a need to operate near other objects and/or incorporate some notion of propellant-optimality or control-effort minimization. In such cases, care is needed to efficiently handle collision-avoidance, plume impingement, sensor line-of-sight, and other complex guidance constraints, which are often non-convex and may depend on time and a mixture of state and control variables. State-of-the-art techniques for collision-free spacecraft proximity operations (both with and without optimality guarantees) include artificial potential function guidance [6, 7], convexification techniques [8], enforcing line-of-sight or approach corridor constraints [9–12], maintaining relative separation [13], satisfying Keep-Out-Zone (KOZ) constraints using mixed-integer (MI) programming [14], and kinodynamic motion planning algorithms [15–18].

Requiring hard assurances of mission safety with respect to a wide variety and number of potential failure modes [19] provides an additional challenge. Often the concept of *passive safety* (safety certifications on zero-control-effort failure trajectories) over a finite horizon is employed to account for the possibility of control failures, though this potentially neglects mission-saving opportunities and fails to certify safety for all time. A less-conservative alternative that more readily adapts to infinite horizons, as we will see, is to use *active safety* in the form of positively-invariant set constraints. For instance, [9] enforces infinite-horizon active safety for a spacecraft by requiring each terminal state to lie on a collision-free orbit of equal period to the target. [16] achieves a similar effect by only planning between waypoints that lie on circular orbits (a more restrictive constraint). Similarly, [20] requires that an autonomous spacecraft maintain access to at least one safe forced equilibrium point nearby. Finally, [21] devises the Safe and Robust Model Predictive Control (MPC) algorithm, which employs invariant feedback tubes about a nominal trajectory (which guarantee resolvability) together with positively-invariant sets (taken about reference safety states) designed to be available at all times over the planning horizon.

The objective of this paper is to design an automated approach to actively-safe spacecraft trajectory optimization for rendezvous and proximity operations near circular orbits, which we model using Clohessy-Wiltshire-Hill (CWH) dynamics. Our approach is to leverage recent advances from the field of robot motion planning, in particular from the area of *sampling-based* motion planning [22]. Several decades of research in the robotics community have shown that sampling-based planning algorithms (dubbed “planners” throughout this paper) show promise for tightly-constrained, high-dimensional optimal control problems such as the one considered in this paper. Sampling-based motion planning essentially entails the breakdown of a complex trajectory control problem into a series of many relaxed, simpler Two-Point Boundary Value Problems (2PBVPs, or “steering” problems) that are subsequently evaluated *a posteriori* for constraint satisfaction and efficiently strung together into a graph (*i.e.*, a tree or roadmap). In this way, complex constraints like obstacle avoidance or plume impingement are decoupled from the generation of subtrajectories (or graph “edges”) between graph states (or “samples”), separating dynamic simulation from constraint checking – a fact we exploit to achieve real-time capability. Critically, this approach avoids the *explicit* construction of the free state space, which is prohibitive in complex planning problems. As a result, sampling-based algorithms can address a large variety of constraints and can provide significant computational benefits with respect to traditional optimal control methods and mixed-integer programming [22]. Furthermore, through a property called *asymptotic optimality* (AO), sampling-based algorithms can be designed to provide guarantees of optimality in the limit that the number of samples taken approaches infinity. This makes sampling-based planners a strong choice for the problem of spacecraft control.

Though the aforementioned works [15–18] on sampling-based planning for spacecraft proximity operations have addressed several components of the safety-constrained, optimal CWH autonomous rendezvous problem, few have addressed the aspect of real-time implementability in conjunction with both a 2-norm propellant-cost metric and active trajectory safety with respect to control failures. This paper seeks to fill this gap. The paper’s central theme is a rigorous proof of asymptotic optimality for a particular sampling-based planner, namely a modified version of the Fast Marching Tree (FMT*) algorithm [23], under impulsive CWH spacecraft dynamics with hard safety constraints.

First, a description of the problem scenario is provided in Section II, along with a formal definition of the 2-norm cost metric that we employ as a proxy for propellant consumption. Section III then follows with a thorough discussion of chaser/target vehicle safety, defining precisely how abort trajectories may be designed under CWH dynamics to deterministically avoid for all future times an ellipsoidal region about the CWH frame origin under a prescribed set of control failures. Next, we proceed in Section IV to our proposed approach employing the modified FMT* algorithm. The section begins with presentation of a conservative approximation to the propellant-cost reachability set, which characterizes the set of states that are “nearby” to a given initial state in terms of propellant use. These sets, bounded by unions of ellipsoidal balls, are then used to show that the modified FMT* algorithm maintains its (asymptotic) optimality when applied to CWH dynamics under the 2-norm cost function. From there, in Section V, the paper presents two techniques for improving motion planning solutions: (i) an analytical technique that can be called both during planning and post-processing to merge Δv -vectors between any pair of concatenated graph edges, and (ii) a continuous trajectory smoothing algorithm, which can reduce the magnitude of Δv -vectors by relaxing the implicit constraint to pass through sample points while still maintaining solution feasibility.

The combination of these tools into a unified framework provides a flexible, general technique for near-circular orbit spacecraft trajectory generation that automatically guarantees bounds on run time and solution quality (propellant cost) while handling a wide variety of (possibly non-convex) state, time, and control constraints. The methodology is demonstrated in Section VI on a single-chaser, single-target scenario simulating a near-field Low Earth Orbit (LEO) approach with hard constraints on total maneuver duration, relative positioning (including keep-out-zone and antenna interference constraints), thruster plume impingement, individual and net Δv -vector magnitudes, and a two-fault thruster stuck-off failure tolerance. The performances of FMT* and the trajectory smoothing techniques are evaluated as a function of sample count and a propellant cost threshold.

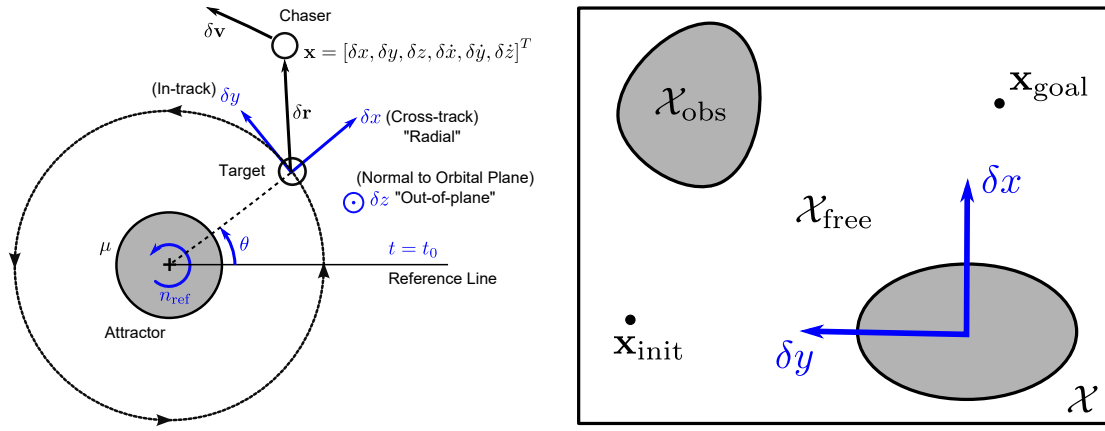
Preliminary versions of this paper appear in [24, 25]. This extended and revised work introduces the following as additional contributions: (i) a more detailed presentation of the FMT* optimality proof, (ii) improved trajectory smoothing techniques, and (iii) a six-dimensional (3-DOF) numerical example demonstrating non-planar LEO rendezvous.

II Problem Formulation

We begin by defining the problem we wish to solve. We model the near-field homing phase and approach for a spacecraft seeking to maneuver near a target that is moving in a well-defined, circular orbit (see Fig. 1a). Let the *state space* $\mathcal{X} \subset \mathbb{R}^d$ represent the d -dimensional region in the target’s Local Vertical, Local Horizontal (LVLH) frame in which the mission is defined, and define the *obstacle region* or \mathcal{X}_{obs} as the set of states within \mathcal{X} that result in mission failure (*e.g.*, states colliding with the target or which lie outside of a specified approach corridor, for example). We then also define the *free space* or $\mathcal{X}_{\text{free}}$ as the complement of \mathcal{X}_{obs} , *i.e.*, states in \mathcal{X} which lie outside of obstacles. As illustrated in Fig. 1b, let \mathbf{x}_{init} represent the chaser spacecraft’s initial state relative to the target, and let $\mathbf{x}_{\text{goal}} \in \mathcal{X}_{\text{goal}}$ be a goal state (a new position/velocity near which the chaser can initiate a docking sequence, a survey maneuver, *etc.*) inside the *goal region* $\mathcal{X}_{\text{goal}}$. Finally, define a *state trajectory* (or simply “trajectory”) as a piecewise-continuous function of time $\mathbf{x}(t) : \mathbb{R} \rightarrow \mathcal{X}$, and let Σ represent the set of all state trajectories. Every state trajectory is implicitly generated by a control trajectory $\mathbf{u}(t) : \mathbb{R} \rightarrow \mathcal{U}$, where \mathcal{U} is the set of controls, through the system dynamics $\dot{\mathbf{x}} = f(\mathbf{x}, \mathbf{u}, t)$, where f is the system’s state transition function. A state trajectory is called a *feasible* solution to the planning problem $(\mathcal{X}_{\text{free}}, t_{\text{init}}, \mathbf{x}_{\text{init}}, \mathbf{x}_{\text{goal}})$ if: (i) it satisfies the boundary conditions $\mathbf{x}(t_{\text{init}}) = \mathbf{x}_{\text{init}}$ and $\mathbf{x}(t_{\text{final}}) = \mathbf{x}_{\text{goal}}$ for some time $t_{\text{final}} > t_{\text{init}}$, (ii) it is *collision-free*; that is, $\mathbf{x}(\tau) \in \mathcal{X}_{\text{free}}$ for all $\tau \in [t_{\text{init}}, t_{\text{final}}]$, and (iii) it obeys all other trajectory constraints, including the system dynamics. The general motion planning problem can then be defined as follows.

Definition 1 (Optimal Planning Problem). Given a planning problem $(\mathcal{X}_{\text{free}}, t_{\text{init}}, \mathbf{x}_{\text{init}}, \mathbf{x}_{\text{goal}})$ and a cost functional $J : \Sigma \times \mathcal{U} \times \mathbb{R} \rightarrow \mathbb{R}_{\geq 0}$, find a feasible trajectory $\mathbf{x}^*(t)$ with associated control trajectory $\mathbf{u}^*(t)$ and time span $t = [t_{\text{init}}, t_{\text{final}}]$ for $t_{\text{final}} \in [t_{\text{init}}, \infty)$ such that $J(\mathbf{x}^*(\cdot), \mathbf{u}^*(\cdot), t) = \min\{J(\mathbf{x}(\cdot), \mathbf{u}(\cdot), t) \mid \mathbf{x}(t) \text{ and } \mathbf{u}(t) \text{ are feasible}\}$. If no such trajectory exists, report failure.

For our particular case, we employ a control-effort cost functional J that considers only the control trajectory $\mathbf{u}(t)$ and the final time t_{final} , which we represent by the notation $J(\mathbf{u}(t), t_{\text{final}})$. Tailoring Definition 1 to impulsively-actuated propellant-optimal motion planning near circular orbits (where here we assume propellant optimality is measured by the 2-norm metric), the spacecraft



(a) Schematic of CWH dynamics, which models relative guidance near a single target in a circular orbit.

(b) A representative motion planning query between feasible states \mathbf{x}_{init} and \mathbf{x}_{goal} .

Fig. 1 Illustration of the CWH planning scenario.

motion planning problem we wish to solve is formulated as:

Given: Initial state $\mathbf{x}_{\text{init}}(t_{\text{init}})$, Goal region $\mathcal{X}_{\text{goal}}$, Free space $\mathcal{X}_{\text{free}}$ (1)

$$\underset{\mathbf{u}(t), t_{\text{final}}}{\text{minimize}} \quad J(\mathbf{u}(t), t_{\text{final}}) = \int_{t_{\text{init}}}^{t_{\text{final}}} \|\mathbf{u}(t)\|_2 dt = \sum_{i=1}^N \|\Delta \mathbf{v}_i\|_2$$

subject to $\mathbf{x}(t_{\text{init}}) = \mathbf{x}_{\text{init}}$

Initial Condition

$\mathbf{x}(t_{\text{final}}) \in \mathcal{X}_{\text{goal}}$

Terminal Condition

$\dot{\mathbf{x}}(t) = f(\mathbf{x}(t), \mathbf{u}(t), t)$

System Dynamics

$\mathbf{x}(t) \in \mathcal{X}_{\text{free}}$ for all $t \in [t_{\text{init}}, t_{\text{final}}]$

Obstacle Avoidance

$\mathbf{g}(\mathbf{x}(t), \mathbf{u}(t), t) \leq 0$

for all $t \in [t_{\text{init}}, t_{\text{final}}]$ Other Constraints

$\mathbf{h}(\mathbf{x}(t), \mathbf{u}(t), t) = 0$

\exists safe $\mathbf{x}_{\text{CAM}}(\tau), \tau > t$ for all $\mathbf{x}(t)$

Active Safety

where t_{init} and t_{final} are the initial and final times, $\mathbf{x}_{\text{CAM}}(\tau)$ refers to an infinite-horizon Collision-Avoidance-Maneuver (CAM), and we restrict our attention to impulsive control laws $\mathbf{u}(t) = \sum_{i=1}^N \Delta \mathbf{v}_i \delta(t - \tau_i)$, where $\delta(\cdot)$ denotes the Dirac delta function, which represent a finite sequence of instantaneous translational burns $\Delta \mathbf{v}_i$ fired at discrete times τ_i (note that the number of burns N is not fixed *a priori*). Though one could consider the set of all possible control laws, it is both theoretically and computationally simpler to optimize over the finite-dimensional search space enabled

by using Δv -vectors; furthermore, such control laws represent the most common forms of propulsion systems used on-orbit, including high-impulse cold-gas and liquid bi-propellant thrusters, and can at least in theory approximate continuous control trajectories in the limit that $N \rightarrow \infty$.

We now elaborate on the objective function and each constraint in turn.

A Cost Functional

A critical component of the spacecraft rendezvous problem is the choice of the cost function. Consistent with the conclusions of [26], we define our cost as the L^1 -norm of the ℓ_p -norm of the control. The best choice for $p \geq 1$ depends on the propulsion system geometry, and on the frame within which $\mathbf{u}(t) = \sum_{i=1}^N \Delta \mathbf{v}_i \delta(t - \tau_i)$ in J is resolved. Minimizing propellant directly requires resolving $\Delta \mathbf{v}_i$ into the spacecraft body-fixed frame; unfortunately, without relaxations, this requires spacecraft attitude \mathbf{q} to be included in our state \mathbf{x} . To avoid this, a standard used throughout the literature and routinely in practical applications is to employ $p = 2$ so that each $\Delta \mathbf{v}_i$ is as short as possible, and optimally allocate the commanded $\Delta \mathbf{v}_i$ to thrusters later (online, once the attitude is known). Though this moves propellant minimization to a separate control allocation step (which we discuss in more detail in Section II E), it greatly simplifies the problem in a practical way without neglecting attitude. Because the cost of Δv -allocation can only grow due to the need to satisfy torque constraints or impulse bounds (*e.g.*, necessitating counter-opposing thrusters to achieve the same net Δv -vector), we are in effect minimizing the best-case, unconstrained propellant use of the spacecraft. As we will show in our numerical experiments, this does not detract significantly from the technique; the coupling of J with $p = 2$ to the actual propellant use through the minimum control-effort thruster Δv allocation problem seems to promote low propellant-cost solutions. Hence (in practice) J serves as a good proxy to propellant use, with the added benefit of independence from propulsion system geometry.

B Boundary Conditions

Sampling-based motion planners generally assume a known initial state \mathbf{x}_{init} and time t_{init} from which planning begins (*e.g.*, the current state of the spacecraft), and define one or more goal regions $\mathcal{X}_{\text{goal}}$ to which guidance is sought. In this paper, we assume the chaser targets only one goal state

$\mathbf{x}_{\text{goal}}^T = [\delta \mathbf{r}_{\text{goal}}^T \ \delta \mathbf{v}_{\text{goal}}^T]$ at a time (“exact convergence,” $\mathcal{X}_{\text{goal}} = \{\mathbf{x}_{\text{goal}}\}$), where $\delta \mathbf{r}_{\text{goal}}$ is the goal position and $\delta \mathbf{v}_{\text{goal}}$ is the goal velocity. During numerical experiments, however, we sometimes permit termination at any state whose position and velocity lie within Euclidean balls $\mathcal{B}(\delta \mathbf{r}_{\text{goal}}, \epsilon_r)$ and $\mathcal{B}(\delta \mathbf{v}_{\text{goal}}, \epsilon_v)$, respectively (“inexact convergence,” $\mathcal{X}_{\text{goal}} = \mathcal{B}(\mathbf{r}_{\text{goal}}, \epsilon_r) \times \mathcal{B}(\mathbf{v}_{\text{goal}}, \epsilon_v)$), where the notation $\mathcal{B}(\mathbf{r}, \epsilon) = \{\mathbf{x} \in \mathcal{X} \mid \|\mathbf{r} - \mathbf{x}\| \leq \epsilon\}$ denotes a ball with center \mathbf{r} and radius ϵ .

C System Dynamics

Because spacecraft proximity operations incorporate significant drift, spatially-dependent external forces, and changes on fast timescales, any realistic solution must obey dynamic constraints; we cannot assume straight-line trajectories. In this paper, we employ the classical Clohessy-Wiltshire-Hill (CWH) equations [27, 28] for impulsive linearized motion about a circular reference orbit at radius r_{ref} about an inverse-square-law gravitational attractor with parameter μ . This model provides a first-order approximation to a chaser spacecraft’s motion relative to a rotating target-centered coordinate system (see Fig. 1). The linearized equations of motion for this scenario as resolved in the Local Vertical, Local Horizontal (LVLH) frame of the target are given by:

$$\delta \ddot{x} - 3n_{\text{ref}}^2 \delta x - 2n_{\text{ref}} \delta \dot{y} = \frac{F_x}{m} \quad (2a)$$

$$\delta \ddot{y} + 2n_{\text{ref}} \delta \dot{x} = \frac{F_y}{m} \quad (2b)$$

$$\delta \ddot{z} + n_{\text{ref}}^2 \delta z = \frac{F_z}{m} \quad (2c)$$

where $n_{\text{ref}} = \sqrt{\frac{\mu}{r_{\text{ref}}^3}}$ is the orbital frequency (mean motion) of the reference spacecraft orbit, m is the spacecraft mass, $\mathbf{F} = [F_x, F_y, F_z]$ is some applied force, and $(\delta x, \delta y, \delta z)$ and $(\delta \dot{x}, \delta \dot{y}, \delta \dot{z})$ represent the cross-track (“radial”), in-track, and out-of-plane relative position and relative velocity, respectively. The CWH model is quite common, and used often for rendezvous and proximity operations in Low Earth Orbit (LEO) and for leader-follower formation flight dynamics.

Defining the state \mathbf{x} as $[\delta x, \delta y, \delta z, \delta \dot{x}, \delta \dot{y}, \delta \dot{z}]^T$ and the applied force-per-unit-mass \mathbf{u} as $\frac{1}{m} \mathbf{F}^T$, the CWH equations can be described by the *linear time-invariant* (LTI) system:

$$\dot{\mathbf{x}} = f(\mathbf{x}, \mathbf{u}, t) = \mathbf{A}\mathbf{x} + \mathbf{B}\mathbf{u} \quad (3)$$

where the dynamics matrix \mathbf{A} and input matrix \mathbf{B} are given by:

$$\mathbf{A} = \begin{bmatrix} 0 & 0 & 0 & 1 & 0 & 0 \\ 0 & 0 & 0 & 0 & 1 & 0 \\ 0 & 0 & 0 & 0 & 0 & 1 \\ 3n_{\text{ref}}^2 & 0 & 0 & 0 & 2n_{\text{ref}} & 0 \\ 0 & 0 & 0 & -2n_{\text{ref}} & 0 & 0 \\ 0 & 0 & -n_{\text{ref}}^2 & 0 & 0 & 0 \end{bmatrix} \quad \mathbf{B} = \begin{bmatrix} 0 & 0 & 0 \\ 0 & 0 & 0 \\ 0 & 0 & 0 \\ 1 & 0 & 0 \\ 0 & 1 & 0 \\ 0 & 0 & 1 \end{bmatrix}.$$

As for any LTI system, we can express the solution to Eq. (3) for any time $t \geq t_0$ using superposition and the convolution integral as $\mathbf{x}(t) = e^{\mathbf{A}(t-t_0)}\mathbf{x}(t_0) + \int_{t_0}^t e^{\mathbf{A}(t-\tau)}\mathbf{B}\mathbf{u}(\tau) d\tau$. The expression $\Phi(t, \tau) \triangleq e^{\mathbf{A}(t-\tau)}$ is called the *state transition matrix*, which importantly provides an analytical mechanism for computing state trajectories that we rely heavily upon in simulations. Note, throughout this work, we shall sometimes represent $\Phi(t, \tau)$ as Φ for brevity when its arguments are understood.

We now specialize the above to the case of N impulsive velocity changes at times $t_0 \leq \tau_i \leq t_f$, for $i \in [1, \dots, N]$, in which case $\mathbf{u}(\tau) = \sum_{i=1}^N \Delta \mathbf{v}_i \delta(\tau - \tau_i)$, where $\delta(y) = \{1 \text{ where } y = 0, \text{ or } 0 \text{ otherwise}\}$ signifies the Dirac-delta distribution. Substituting for Φ and $\mathbf{u}(\tau)$, this yields:

$$\begin{aligned} \mathbf{x}(t) &= \Phi(t, t_0)\mathbf{x}(t_0) + \int_{t_0}^t \Phi(t, \tau)\mathbf{B} \left(\sum_{i=1}^N \Delta \mathbf{v}_i \delta(\tau - \tau_i) \right) d\tau \\ &= \Phi(t, t_0)\mathbf{x}(t_0) + \sum_{i=1}^N \int_{t_0}^t \Phi(t, \tau)\mathbf{B}\Delta \mathbf{v}_i \delta(\tau - \tau_i) d\tau, \end{aligned}$$

where on the second line we used the linearity of the integral operator. By the sifting property of δ , denoting N_t as the number of burns applied from t_0 up to time t , we have for all times $t \geq t_0$ the following expression for the impulsive solution to Eq. (3):

$$\mathbf{x}(t) = \Phi(t, t_0)\mathbf{x}(t_0) + \sum_{i=1}^{N_t} \Phi(t, \tau_i)\mathbf{B}\Delta \mathbf{v}_i \quad (5a)$$

$$= \Phi(t, t_0)\mathbf{x}(t_0) + \underbrace{\left[\Phi(t, \tau_1)\mathbf{B} \dots \Phi(t, \tau_{N_t})\mathbf{B} \right]}_{\triangleq \Phi_v(t, \{\tau_i\}_i)} \underbrace{\begin{bmatrix} \Delta \mathbf{v}_1 \\ \vdots \\ \Delta \mathbf{v}_{N_t} \end{bmatrix}}_{\triangleq \Delta \mathbf{V}} \quad (5b)$$

$$= \Phi(t, t_0)\mathbf{x}(t_0) + \Phi_v(t, \{\tau_i\}_i)\Delta \mathbf{V}. \quad (5c)$$

Throughout this paper, the notations $\Delta \mathbf{V}$ for the stacked Δv -vector and $\Phi_v(t, \{\tau_i\}_i)$ for the aggregated impulse state transition matrix (or simply Φ_v for short, when the parameters t and $\{\tau_i\}_i$ are clear) implicitly imply only those burns i occurring before time t .

D Obstacle Avoidance

Obstacle avoidance is imposed by requiring the spacecraft trajectory $\mathbf{x}(t)$ to stay within $\mathcal{X}_{\text{free}}$ (or, equivalently, outside of the obstacle region \mathcal{X}_{obs}) – typically a difficult non-convex constraint. For CWH proximity operations, \mathcal{X}_{obs} might include those states that result in a collision with a neighboring object, all positions which lie outside of a given approach corridor, all velocities violating a given relative guidance law, *etc.* In our numerical experiments, we assume \mathcal{X}_{obs} includes an ellipsoidal Keep Out Zone (KOZ) enclosing the target spacecraft centered at the origin and a conical nadir-pointing region that approximates its antenna beam pattern – this both enforces collision-avoidance and prevents the chaser from interfering with the target’s communications.

Note that according to the definition of $\mathcal{X}_{\text{free}}$, this also requires the solution $\mathbf{x}(t)$ to stay within the confines of \mathcal{X} (CWH system dynamics do not guarantee that state trajectories will lie in \mathcal{X} despite the fact that their endpoints do). Though not strictly necessary in practice, if $\mathcal{X}_{\text{free}}$ is defined to mark the extent of reliable sensor readings or the boundary inside which CWH equation linearity assumptions hold, then this can be a useful constraint to enforce.

E Other Trajectory Constraints

Many other types of constraints may be included to encode additional restrictions on state and control trajectories, which we represent here by a set of inequality constraints \mathbf{g} and equality constraints \mathbf{h} (note that \mathbf{g} and \mathbf{h} denote vector functions). To illustrate the flexibility of the

sampling-based planning approach, we encode the following into constraints \mathbf{g} (for brevity, we omit their exact representation, which is straightforward based on vector geometry):

$$\begin{aligned}
T_{\text{plan},\min} &\leq t_{\text{final}} - t_{\text{init}} \leq T_{\text{plan},\max} && \text{Plan Duration Bounds} \\
\Delta \mathbf{v}_i &\in \mathcal{U}(\mathbf{x}(\tau_i)) && \text{for all } i = [1, \dots, N] \quad \text{Control Feasibility} \\
\bigcup_{k \in [1, \dots, K]} \mathcal{P}_{ik}(-\Delta \hat{\mathbf{v}}_{ik}, \beta_{\text{plume}}, H_{\text{plume}}) \cap \mathbb{S}_{\text{target}} &= \emptyset && \text{for all } i = [1, \dots, N] \quad \text{Plume Impingement}
\end{aligned}$$

Here $0 \leq T_{\text{plan},\min} < T_{\text{plan},\max}$ represent minimum and maximum motion plan durations, $\mathcal{U}(\mathbf{x}(\tau_i))$ is the admissible *control set* corresponding to state $\mathbf{x}(\tau_i)$, \mathcal{P}_{ik} is the exhaust plume emanating from thruster k of the chaser spacecraft while executing burn $\Delta \mathbf{v}_i$ at time τ_i , and $\mathbb{S}_{\text{target}}$ is the target spacecraft circumscribing sphere. We motivate each constraint in turn.

a Plan Duration Bounds Plan duration bounds facilitate the inclusion of rendezvous windows based on the epoch of the chaser at $\mathbf{x}_{\text{init}}(t_{\text{init}})$; such windows might be determined by illumination requirements, grounds communication opportunities, or mission timing restrictions, for example. $T_{\text{plan},\max}$ may also be used to ensure the errors incurred by our linearized CWH model, which grow with time, do not exceed acceptable tolerances.

b Control Feasibility Control set constraints are intended to encapsulate limitations on control authority imposed by propulsive actuators and their geometric distribution about the spacecraft. For example, given the maximum burn magnitude $0 < \Delta v_{\max}$, the constraint:

$$\|\Delta \mathbf{v}_i\|_2 \leq \Delta v_{\max} \text{ for all } i = [1, \dots, N] \quad (6)$$

might be used to represent an upper bound on the impulse range achievable by a gimbaled thruster system that is able to direct thrust freely in all directions. In our case, we use $\mathcal{U}(\mathbf{x}(\tau_i))$ to represent all commanded net Δv -vectors that (i) satisfy the constraint Eq. (6) above, and also (ii) can be successfully allocated to thrusters along trajectory $\mathbf{x}(t)$ at time τ_i according to a simple minimum-control effort thruster allocation problem (a straightforward linear program (LP) [29]). To keep the paper self-contained, we repeat the problem here and in our notation. Let $\Delta \mathbf{v}_i|_{\text{bf}}$ and $\mathbf{M}_i|_{\text{bf}}$ be the desired net Δv and moment vectors at burn time τ_i , resolved in the body-fixed frame

according to attitude $\mathbf{q}(\tau_i)$ (we henceforth drop the bar, for brevity). Note the attitude $\mathbf{q}(\tau_i)$ must either be included in the state $\mathbf{x}(\tau_i)$ or be derived from it, as is assumed in this paper by imposing (along nominal trajectories) a nadir-pointing attitude profile for the chaser spacecraft. Let $\Delta v_{ik} = \|\Delta \mathbf{v}_{ik}\|_2$ be the Δv -magnitude allocated to thruster k , which generates an impulse in direction $\Delta \hat{\mathbf{v}}_{ik}$ at position $\boldsymbol{\rho}_{ik}$ from the spacecraft center-of-mass (both are constant vectors if resolved in the body-fixed frame). Finally, to account for the possibility of on or off thrusters, let η_{ik} be equal to 1 if thruster k is available for burn i , or 0 otherwise. Then the minimum-effort control allocation problem can be represented as:

$$\begin{aligned}
\text{Given:} \quad & \text{On-off flags } \eta_{ik}, \text{ thruster positions } \boldsymbol{\rho}_{ik}, \text{ thruster axes } \Delta \hat{\mathbf{v}}_{ik}, & (7) \\
& \text{commanded } \Delta v\text{-vector } \Delta \mathbf{v}_i, \text{ and commanded moment vector } \mathbf{M}_i \\
\text{minimize} \quad & \sum_{k=1}^K \Delta v_{ik} \\
\text{subject to} \quad & \sum_{k=1}^K \Delta \hat{\mathbf{v}}_{ik} (\eta_{ik} \Delta v_{ik}) = \Delta \mathbf{v}_i & \text{Net } \Delta v\text{-Vector Allocation} \\
& \sum_{k=1}^K (\boldsymbol{\rho}_{ik} \times \Delta \hat{\mathbf{v}}_{ik}) (\eta_{ik} \Delta v_{ik}) = \mathbf{M}_i & \text{Net Moment Allocation} \\
& \Delta v_{\min,k} \leq \Delta v_{ik} \leq \Delta v_{\max,k} & \text{Thruster } \Delta v \text{ Bounds}
\end{aligned}$$

where $\Delta v_{\min,k}$ and $\Delta v_{\max,k}$ represent minimum and maximum impulse limits on thruster k (due to actuator limitations, minimum impulse bit, pulse-width constraints, or maximum on-time restrictions, for example). Because Δv is directly-proportional to thrust through the Tsiolkovsky rocket equation, the formulation above is directly analogous to minimum-propellant consumption; as discussed in Section II A, by using control trajectories that minimize commanded Δv -vector lengths $\|\Delta \mathbf{v}_i\|$, we can drive propellant use downwards as much as possible subject to our thrust bounds and net torque constraints. In this work, we set $\mathbf{M}_i = \mathbf{0}$ to enforce torque-free burns and minimize the disturbance to our assumed attitude trajectory $\mathbf{q}(t)$.

Note that we do not consider a minimum norm constraint in Eq. (6) for $\Delta \mathbf{v}_i$. As discussed in Section II A, $\|\Delta \mathbf{v}_i\|$ is only a proxy for the true propellant cost computed from the thrust allocation problem (Eq. (7)). The value of the norm bound Δv_{\max} may be computed from the thruster limits

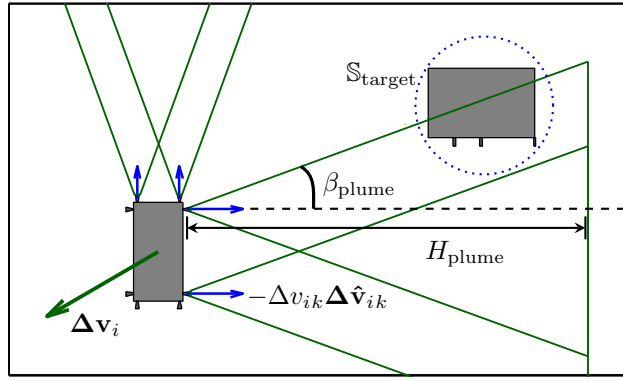


Fig. 2 Illustration of exhaust plume impingement from thruster firings.

$\Delta v_{\min,k}$, $\Delta v_{\max,k}$ and knowledge of the thruster configuration.

c Plume Impingement Impingement of thruster exhaust on neighboring spacecraft can lead to dire consequences, including destabilizing effects on attitude caused by exhaust gas pressure, degradation of sensitive optical equipment and solar arrays, and unexpected thermal loading [30]. To take this into account, we generate representative exhaust plumes at the locations of each thruster firing. For burn i occurring at time τ_i , a right circular cone is generated with axis $-\Delta\hat{\mathbf{v}}_{ik}$, half-angle β_{plume} , and height H_{plume} at each *active* thruster k ($\eta_{ik} = 1$) for which its allocated thrust Δv_{ik}^* is non-zero, as determined by the solution to Eq. (7). Intersections are checked with the target spacecraft circumscribing sphere, $\mathbb{S}_{\text{target}}$, which is used as a more efficiently-verified, conservative approximation to the exact target geometry. For an illustration, see Fig. 2.

d Other Constraints Other constraints may easily be added. Solar array shadowing, pointing constraints, approach corridor constraints, *etc.*, all fit within the framework, and may be represented as additional inequality or equality constraints. For additional examples, refer to [31].

F Active Safety

An additional feature we include in our work is the concept of *active safety*, in which we require the target spacecraft to maintain a feasible Collision Avoidance Maneuver (CAM) to a safe higher or lower circular orbit from every point along its solution trajectory in the event that any mission-threatening control degradations such as stuck-off thrusters (as in Fig. 3) take place. This reflects our previous work [24], and is detailed more thoroughly in Section III.

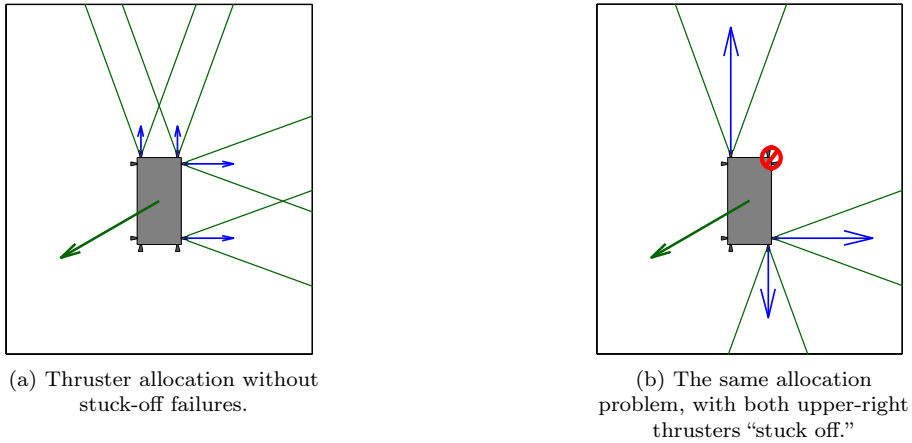


Fig. 3 Changes to torque-free control allocation in response to thruster failures.

III Vehicle Safety under CWH Dynamics

In this section, we describe a general strategy for handling the active safety constraints introduced in Eq. (1) and Section II F, whereby we seek to deterministically certify our solution trajectory with respect to thruster “stuck-off” failures up to a given fault-tolerance but without compromising real-time implementability. As will be motivated, the idea is to embed the escape trajectory generation process together with positively-invariant set safety constraints into the sampling routine of sampling-based motion planners. Due to the propellant-limited nature of many spacecraft proximity operations missions, emphasis is placed on finding minimum- Δv escape maneuvers in order to improve mission reattempt opportunities. We prioritize *active safety* measures (which allow actuated Collision Avoidance Maneuvers or CAMs) over passive safety guarantees (which shut off all thrusters and restrict the system to zero control) in order to broaden the search space for abort trajectories and thereby allow better performance during the nominal mission. We emulate the rendezvous design process taken by Barbee et al. [32], but numerically optimize propellant consumption and remove much of its reliance on user intuition by automating the satisfaction of safety constraints.

Consistent with the notions proposed by Schouwenaars et al. [33], Fehse [34, 4.1.2], and Fraichard [35], the definition of vehicle safety in this paper is taken as the following:

Definition 2 (Vehicle Safety). A vehicle state is *safe* if and only if there exists, under the worst-possible environment and failure conditions, a collision-free, dynamically-feasible trajectory satisfying the constraints that navigates the vehicle to a set of states in which it can remain indefinitely.

Note *indefinitely* (or sufficiently-long for all practical purposes under the accuracy of the dynamics model) is a critical component of the definition. Trajectories without infinite-horizon safety guarantees can ultimately violate constraints [9], thereby posing a risk that can defeat the purpose of using a hard guarantee in the first place. For this reason, we impose safety constraints over an infinite-horizon (or, as we will show using invariant sets, an *effectively* infinite horizon).

Consider the scenario described in Section II for a spacecraft with nominal state trajectory $\mathbf{x}(t) \in \mathcal{X}$ and control trajectory $\mathbf{u}(t) \in \mathcal{U}(\mathbf{x}(t))$ evolving over time t in time span $\mathcal{T} = [t_{\text{init}}, \infty)$. Let $\mathcal{T}_{\text{fail}} \subseteq \mathcal{T}$ represent the set of potential failure times we wish to certify (for instance, a set of prescribed burn times $\{\tau_i\}$, the final approach phase $\mathcal{T}_{\text{approach}}$, or the entire maneuver span \mathcal{T}). When a failure occurs, control authority is lost through a reduction in actuator functionality, negatively impacting system controllability. Let $\mathcal{U}_{\text{fail}}(\mathbf{x}) \subset \mathcal{U}(\mathbf{x})$ represent the new control set, where we assume that $\mathbf{0} \in \mathcal{U}_{\text{fail}}$ for all \mathbf{x} (*i.e.*, we assume that no actuation is always a feasible option). Mission safety is commonly imposed in two different ways [34, 4.4]:

- *Passive Safety*: For all $t_{\text{fail}} \in \mathcal{T}_{\text{fail}}$, ensure that $\mathbf{x}_{\text{CAM}}(t)$ satisfies Definition 2 with $\mathbf{u}_{\text{CAM}}(t) = \mathbf{0}$ for all $t \geq t_{\text{fail}}$. For spacecraft, this means its coasting arc from the point of failure must be safe for all future time (though practically this is imposed only over a finite horizon).
- *Active Safety*: For all $t_{\text{fail}} \in \mathcal{T}_{\text{fail}}$ and failure modes $\mathcal{U}_{\text{fail}}$, design actuated collision avoidance maneuvers $\mathbf{x}_{\text{CAM}}(t)$ to satisfy Definition 2 with $\mathbf{u}_{\text{CAM}}(t) \in \mathcal{U}_{\text{fail}}$ for all $t \geq t_{\text{fail}}$, where $\mathbf{u}_{\text{CAM}}(t)$ is not necessarily restricted to $\mathbf{0}$.

In much of the literature, only passive safety is considered out of a need for tractability (to avoid verification over a combinatorial explosion of failure mode possibilities) and in order to capture the common failure mode in which control authority is lost completely. Though considerably simpler to implement, this approach potentially neglects many mission-saving control policies.

A Positively-Invariant Set Constraints

Instead of evaluating trajectory safety for all future times $t \geq t_{\text{fail}}$, it is generally more practical to consider finite-time solutions starting at $\mathbf{x}(t_{\text{fail}})$ that terminate at a point inside a safe positively invariant set $\mathcal{X}_{\text{invariant}}$. If the maneuver is safe and the invariant set is safe for all time, then safety

of the spacecraft is assured.

Definition 3 (Positively Invariant Set). A set $\mathcal{X}_{\text{invariant}}$ is positively-invariant with respect to the autonomous system $\dot{\mathbf{x}}_{\text{CAM}} = f(\mathbf{x}_{\text{CAM}})$ if and only if $\mathbf{x}_{\text{CAM}}(t_{\text{fail}}) \in \mathcal{X}_{\text{invariant}}$ implies $\mathbf{x}_{\text{CAM}}(t) \in \mathcal{X}_{\text{invariant}}$ for all $t \geq t_{\text{fail}}$.

This yields the following definition for finite-time verification of trajectory safety:

Definition 4 (Finite-Time Trajectory Safety Verification). For all $t_{\text{fail}} \in \mathcal{T}_{\text{fail}}$ and for all $\mathcal{U}_{\text{fail}}(\mathbf{x}(t_{\text{fail}})) \subset \mathcal{U}(\mathbf{x}(t_{\text{fail}}))$, there exists $\{\mathbf{u}(t), t \geq t_{\text{fail}}\} \in \mathcal{U}_{\text{fail}}(\mathbf{x}(t_{\text{fail}}))$ and $T_h > t_{\text{fail}}$ such that $\mathbf{x}(t)$ is feasible for all $t_{\text{fail}} \leq t \leq T_h$ and $\mathbf{x}(T_h) \in \mathcal{X}_{\text{invariant}} \subseteq \mathcal{X}_{\text{free}}$,

where T_h is some finite safety verification horizon time. Though in principle any *safe* positively-invariant set $\mathcal{X}_{\text{invariant}}$ is acceptable, not just any will do in practice; in real-world scenarios, unstable trajectories caused by model uncertainties could cause state divergence towards configurations whose safety has not been verified. Hence care must be taken to use only *stable* positively-invariant sets.

Combining Definition 4 with our constraints in Eq. (1) from Section II, spacecraft trajectory safety after a failure at $\mathbf{x}(t_{\text{fail}}) = \mathbf{x}_{\text{fail}}$ can be expressed in its full generality as the following optimization problem in decision variables $T_h \in [t_{\text{fail}}, \infty)$, $\mathbf{x}_{\text{CAM}}(t)$, and $\mathbf{u}_{\text{CAM}}(t)$, for $t \in [t_{\text{fail}}, T_h]$:

Given: Failure state $\mathbf{x}_{\text{fail}}(t_{\text{fail}})$, failure control set $\mathcal{U}_{\text{fail}}(\mathbf{x}_{\text{fail}})$, the free space $\mathcal{X}_{\text{free}}$, (8)

a safe, stable invariant set $\mathcal{X}_{\text{invariant}}$, and a fixed number of impulses N

$$\underset{\substack{\mathbf{u}_{\text{CAM}}(t) \in \mathcal{U}_{\text{fail}}(\mathbf{x}_{\text{fail}}), \\ T_h, \mathbf{x}_{\text{CAM}}(t)}}{\text{minimize}} \quad J(\mathbf{x}_{\text{CAM}}(t), \mathbf{u}_{\text{CAM}}(t), t) = \int_{t_{\text{fail}}}^{T_h} \|\mathbf{u}_{\text{CAM}}(t)\|_2 dt = \sum_{i=1}^N \|\Delta \mathbf{v}_{\text{CAM}, i}\|_2$$

subject to $\dot{\mathbf{x}}_{\text{CAM}}(t) = f(\mathbf{x}_{\text{CAM}}(t), \mathbf{u}_{\text{CAM}}(t), t)$ System Dynamics

$\mathbf{x}_{\text{CAM}}(t_{\text{fail}}) = \mathbf{x}_{\text{fail}}$ Initial Condition

$\mathbf{x}_{\text{CAM}}(T_h) \in \mathcal{X}_{\text{invariant}}$ Safe Termination

$\mathbf{x}_{\text{CAM}}(t) \in \mathcal{X}_{\text{free}}$ for all $t \in [t_{\text{fail}}, T_h]$ Obstacle Avoidance

$\mathbf{g}(\mathbf{x}_{\text{CAM}}, \mathbf{u}_{\text{CAM}}, t) \leq 0$ for all $t \in [t_{\text{fail}}, T_h]$ Other Constraints

$\mathbf{h}(\mathbf{x}_{\text{CAM}}, \mathbf{u}_{\text{CAM}}, t) = 0$

This is identical to Eq. (1), except that now under failure mode $\mathcal{U}_{\text{fail}}(\mathbf{x}_{\text{fail}})$ we abandon the attempt to terminate at a goal state in $\mathcal{X}_{\text{goal}}$ and instead replace it with a constraint to terminate at a safe, stable positively-invariant set $\mathcal{X}_{\text{invariant}}$. We additionally neglect any timing constraints encoded in \mathbf{g} as we are no longer concerned with our original rendezvous. Typically any feasible solution is sought following a failure, in which case one may use $J = 1$. However, to enhance the possibility of mission recovery, we assume the same minimum-propellant 2-norm cost function as before, but with the exception that here, as we will motivate, we use a single-burn strategy with $N = 1$.

B Fault-Tolerant Safety Strategy

The difficulty of solving the finite-time trajectory safety problem lies in the fact that a feasible solution must be found for *all* possible failure times (typically assumed to be any time during the mission) as well as for *all* possible failures. To illustrate, for an F -fault tolerant spacecraft with K control components (thrusters, momentum wheels, CMGs, *etc.*) that we each model as either “operational” or “failed,” this yields a total of $N_{\text{fail}} = \sum_{f=0}^F \binom{K}{f} = \sum_{f=0}^F \frac{K!}{(K-f)!f!}$ possible optimization problems that must be solved for every time t_{fail} along the nominal trajectory. By any standard, this is intractable, and hence explains why so often *passive* safety guarantees are selected (requiring only one control configuration check instead of N_{fail} , since we prescribe $\mathbf{u}_{\text{CAM}} = \mathbf{0}$ which must lie in $\mathcal{U}_{\text{fail}}$ given our assumption. This is analogous to setting $f = K$ with $F \triangleq K$). One idea for simplifying the problem while still satisfying safety (the constraints of Eq. (8)) consists of the following strategy:

Definition 5 (Fault-Tolerant Active Safety Strategy). As a conservative solution to the optimization problem in Eq. (8), it is sufficient (but not necessary) to implement the following procedure:

1. From each $\mathbf{x}(t_{\text{fail}})$, prescribe a Collision-Avoidance Maneuver (CAM) policy Π_{CAM} that gives a horizon time T_h and escape control sequence $\mathbf{u}_{\text{CAM}} = \Pi_{\text{CAM}}(\mathbf{x}(t_{\text{fail}}))$ designed to automatically satisfy $\mathbf{u}_{\text{CAM}}(\tau) \subset \mathcal{U}$ for all $t_{\text{fail}} \leq \tau \leq T_h$ and $\mathbf{x}(T_h) \in \mathcal{X}_{\text{invariant}}$.
2. For each failure mode $\mathcal{U}_{\text{fail}}(\mathbf{x}(t_{\text{fail}})) \subset \mathcal{U}(\mathbf{x}(t_{\text{fail}}))$ up to tolerance F , determine if the control law is feasible; that is, see if $\mathbf{u}_{\text{CAM}} = \Pi_{\text{CAM}}(\mathbf{x}(t_{\text{fail}})) \subset \mathcal{U}_{\text{fail}}$ for the particular failure in question.

This effectively removes decision variables \mathbf{u}_{CAM} from Eq. (8), allowing simple numerical integration for satisfaction of the dynamic constraints and a straightforward *a posteriori* verification of the other trajectory constraints (inclusion in $\mathcal{X}_{\text{free}}$, and satisfaction of constraints \mathbf{g} and \mathbf{h}). This checks if the prescribed CAM, guaranteed to provide a safe escape route, can actually be accomplished in the given failure situation. The approach is conservative due to the fact that the control law is imposed and not derived; however, the advantage is a greatly simplified optimal control problem with difficult-to-handle constraints relegated to *a posteriori* checks — exactly identical to the way that steering trajectories are derived and verified during the planning process of sampling-based planning algorithms. Note that formal definitions of safety require that this be satisfied for all possible failure modes of the spacecraft; we do not avoid the combinatorial explosion of N_{fail} . However, each instance of problem Eq. (8) is greatly simplified, and with F typically at most 3, the problem remains tractable. The difficult part, then, lies in computing Π_{CAM} , but this can easily be generated in an offline fashion. Hence, the strategy should work well for vehicles with difficult, non-convex objective functions and constraints, as is exactly the case for CWH proximity operations.

Note, it is always possible to reduce this approach to the (more-conservative) definition of “passive safety” that has traditionally been seen in the literature by choosing some finite horizon T_h and setting $\mathbf{u}_{\text{CAM}} = \Pi_{\text{CAM}}(\mathbf{x}(t_{\text{fail}})) = \mathbf{0}$ for all potential failure times $t_{\text{fail}} \in \mathcal{T}_{\text{fail}}$.

C Safety in CWH Dynamics

We now specialize these ideas to proximity operations under impulsive CWH dynamics. Because many missions require stringent avoidance (prior to final approach and docking phase, for example), it is quite common for a “Keep-Out Zone” (KOZ) \mathcal{X}_{KOZ} , typically ellipsoidal in shape, to be defined about the target in the CWH frame. Throughout its approach, the chaser must certify that it will not enter this KOZ under any circumstance up to a specified thruster fault tolerance F . Per Definition 4, this necessitates a search for a safe invariant set for finite-time escape along with, as outlined by Definition 5, the definition of an escape policy Π_{CAM} , which we describe next.

For mission safety following a failure under CWH dynamics, Definition 4 requires us to find a terminal state in an invariant set $\mathcal{X}_{\text{invariant}}$ entirely contained within the free state space $\mathcal{X}_{\text{free}}$. As will be motivated, we choose for $\mathcal{X}_{\text{invariant}}$ the set of circularized orbits whose planar projections lie outside of the radial band spanned by the KOZ. Circular orbits are stable (assuming Keplerian motion, which neglects perturbations that *can* create unstable orbital changes – likely not an unreasonable assumption as presumably the *difference* in chaser/target perturbation responses matters more), accessible (given the proximity of the chaser to the target’s circular orbit), and passively safe (once reached, provided that they do not intersect the KOZ). In the planar case, this set of safe circularized orbits can fortunately be identified by inspection; as can be seen in Fig. 4, we require only that the orbital radius lie outside of the KOZ radial band; otherwise circularization would result in an eventual collision, either in the short-term or after nearly one full synodic period – a violation of Definition 2. Such a region is called a zero-thrust “Region of Inevitable Collision (RIC),” which we denote as \mathcal{X}_{ric} , whose complement $\mathcal{X}_{\text{invariant}}$ can be used to terminate planar escape maneuvers. For the non-planar case, we can conservatively extend this result by considering only those circular orbits whose planar orbit projection avoids \mathcal{X}_{ric} . See Eqs. (9)–(11) for a mathematical description:

$$\mathcal{X}_{\text{KOZ}} = \left\{ \mathbf{x} \mid \mathbf{x}^T \mathbf{E} \mathbf{x} \geq 1, \text{ where } \mathbf{E} = \text{diag} \left(\rho_{\delta x}^{-2}, \rho_{\delta y}^{-2}, \rho_{\delta z}^{-2}, 0, 0, 0 \right), \text{ with } \rho_i \text{ representing} \right. \quad (9)$$

the ellipsoidal KOZ semi-axis in the i -th LVLH frame axis direction.}

$$\mathcal{X}_{\text{ric}} = \left\{ \mathbf{x} \mid |\delta x| < \rho_{\delta x}, \delta \dot{x} = 0, \delta \dot{y} = -\frac{3}{2} n_{\text{ref}} \delta x \right\} \supset \mathcal{X}_{\text{KOZ}} \quad (10)$$

$$\mathcal{X}_{\text{invariant}} = \left\{ \mathbf{x} \mid |\delta x| \geq \rho_{\delta x}, \delta \dot{x} = 0, \delta \dot{y} = -\frac{3}{2} n_{\text{ref}} \delta x \right\} = \mathcal{X}_{\text{ric}}^c \quad (11)$$

In short, our CAM policy to safely escape from a state \mathbf{x} at which the spacecraft arrives (possibly under failures) at time t_{fail} consists of the following:

1. Coast from $\mathbf{x}(t_{\text{fail}})$ to some new $T_h > t_{\text{fail}}$ such that $\mathbf{x}_{\text{CAM}}(T_h^-)$ lies at a position in $\mathcal{X}_{\text{invariant}}$.

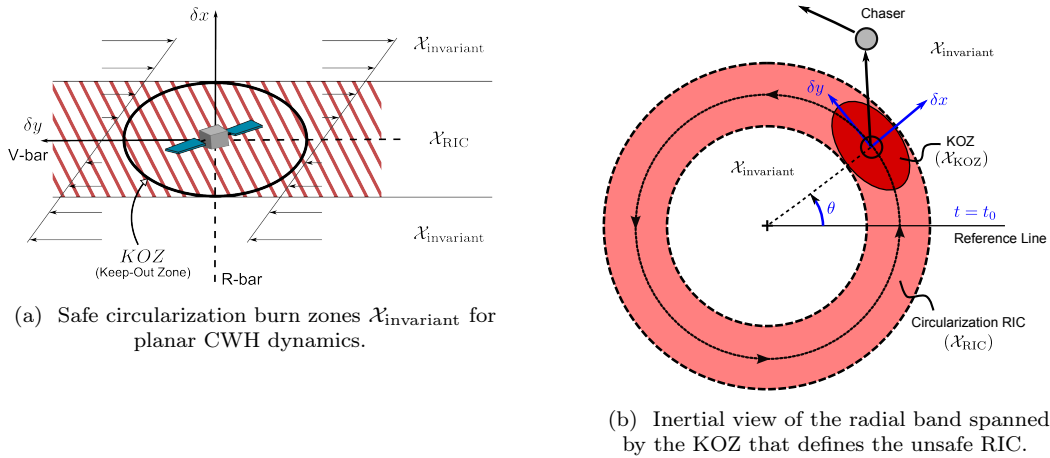


Fig. 4 Visualizing the safe and unsafe circularization regions used by the CAM safety policy.

2. Circularize the orbit at $\mathbf{x}_{\text{CAM}}(T_h)$ such that $\mathbf{x}_{\text{CAM}}(T_h^+) \in \mathcal{X}_{\text{invariant}}$.
3. Coast along the new orbit (horizontal drift along the in-track axis in the CWH relative frame) in $\mathcal{X}_{\text{invariant}}$ until allowed to continue the mission (*e.g.*, after approval from ground operators).

2 Determining the Circularization Time, T_h

In the event of a thruster failure at state $\mathbf{x}(t_{\text{fail}})$ that requires an emergency CAM, the time $T_h > t_{\text{fail}}$ at which to attempt a circularization maneuver after coasting from $\mathbf{x}(t_{\text{fail}})$ becomes a degree of freedom. As we intend to maximize the recovery chances of the chaser after a failure, we choose T_h so as to minimize the cost of the circularization burn $\Delta \mathbf{v}_{\text{circ}}$, whose magnitude we denote Δv_{circ} . Details on the approach, which can be solved analytically, can be found in Appendix A.

3 Verifying CAM Policy Feasibility

Once the circularization time T_h is determined, feasibility of the escape trajectory under every possible failure configuration at $\mathbf{x}(t_{\text{fail}})$ must be assessed in order to declare a particular CAM as actively-safe. To show this, the constraints of Section II must be evaluated under every combination of “stuck-off” thrusters (up to fault tolerance F), *with the exception of KOZ avoidance* as this is embedded into the CAM design process. Fortunately, given our particular constraints encoded in Eq. (8) and described in Section II E (static in the CWH LVLH frame and independent of the

arrival time t_{fail}), assuming additionally that the position of the target is known *a priori* (fixed at the origin) and that the attitude $\mathbf{q}(t)$ of the chaser is specified as a function of our state $\mathbf{x}(t)$, we may evaluate CAM trajectory feasibility (control allocation feasibility, plume impingement, antenna lobe avoidance, *etc.*) in an offline fashion. Better still, we need only evaluate the safety of arriving at \mathbf{x} once; this means the *active* safety of a particular state \mathbf{x} can be cached — a fact we will make extensive use of in the design of our planning algorithm.

IV Planning Algorithm and Theoretical Characterization

With the proximity operations scenario established, we are now in position to describe our approach. As previously described, the constraints that must be satisfied in Eq. (1) are diverse, complex, and difficult to satisfy numerically. In this section, we propose a guidance algorithm to solve this problem, followed by a detailed proof of its optimality with regard to the 2-norm propellant-cost metric J under impulsive CWH dynamics. As will be seen, the proof relies on an understanding of: (i) the steering connections between sampled points assuming no obstacles or other trajectory constraints, and (ii) the nearest-neighbors or *reachable* states from a given state. We hence start by characterizing these two concepts, in Sections IV A and IV B respectively. We then proceed to the algorithm presentation (Section IV C) and its theoretical characterization (Section IV D).

A The Steering Problem

In this section, we consider the *unconstrained* minimal propellant 2-point boundary value problem (2PBVP) or “steering problem” between an initial state \mathbf{x}_0 and a final state \mathbf{x}_f within the CWH dynamics model. Solutions to these steering problems provide the local building blocks from which we construct solutions to the more complicated problem formulation in Eq. (1). Steering solutions serve two main purposes: (i) they represent a class of short-horizon controlled trajectories that are filtered online for constraint satisfaction and efficiently strung together into a state space-spanning graph (*i.e.*, a tree or roadmap), and (ii) the costs of steering trajectories are used to inform the graph construction process by identifying the unconstrained “nearest neighbors” as edge candidates. Because these problems can be expressed independently of the arrival time t_0 (as will be shown), our solution algorithm does not need to solve these problems *online*; the solutions between every pair

of samples can be precomputed and stored prior to receiving a motion query. Hence the 2PBVP presented here need not be solved quickly. However, we mention techniques here for speed-ups due to the reliance of our smoothing algorithm (Algorithm 2) on a fast solution method.

Substituting our boundary conditions into Eq. (5), evaluating at $t = t_f$, and rearranging, we seek a stacked burn vector $\Delta \mathbf{V}$ such that:

$$\Phi_v(t_f, \{\tau_i\}_i) \Delta \mathbf{V} = \mathbf{x}_f - \Phi(t_f, t_0) \mathbf{x}_0, \quad (12)$$

for some number N of burn times $\tau_i \in [t_0, t_f]$. Formulating this as an optimal control problem that minimizes our 2-norm cost functional (as a proxy for the actual propellant consumption, as described in Section II A), we wish to solve:

$$\begin{aligned} \text{Given:} \quad & \text{Initial state } \mathbf{x}_0, \text{ final state } \mathbf{x}_f, \text{ burn magnitude bound } \Delta v_{\max}, & (13) \\ & \text{and maneuver duration bound } T_{\max} \\ \text{minimize} \quad & \sum_{i=1}^N \|\Delta \mathbf{v}_i\|_2 \\ \text{subject to} \quad & \Phi_v(t_f, \{\tau_i\}_i) \Delta \mathbf{V} = \mathbf{x}_f - \Phi(t_f, t_0) \mathbf{x}_0. & \text{Dynamics/Boundary Conditions} \\ & 0 \leq t_f - t_0 \leq T_{\max} & \text{Maneuver Duration Bounds} \\ & t_0 \leq \tau_i \leq t_f \quad \text{for burns } i & \text{Burn Time Bounds} \\ & \|\Delta \mathbf{v}_i\|_2 \leq \Delta v_{\max} \quad \text{for burns } i & \text{Burn Magnitude Bounds} \end{aligned}$$

Notice that this is a relaxed version of the original problem presented as Eq. (1), with only its boundary conditions, dynamic constraints, and control norm bound. As it stands, due to the nonlinearity of the dynamics with respect to τ_i , t_f and N , Eq. (13) is non-convex and inherently difficult to solve. However, we can make the problem tractable if we make a few assumptions. Given that we plan to string many steering trajectories together to form our overall solution, let us ensure they represent the most primitive building blocks possible such that their concatenation will adequately represent any arbitrary trajectory. Set $N = 2$ (the smallest number of burns required to transfer between any pair of arbitrary states, as it makes $\Phi_v(t_f, \{\tau_i\}_i)$ square) and select burn times

$\tau_1 = t_0$ and $\tau_2 = t_f$ (which automatically satisfy our burn time bounds). This leaves $\Delta \mathbf{v}_1 \in \mathbb{R}^{d/2}$ (an intercept burn applied just after \mathbf{x}_0 at time t_0), $\Delta \mathbf{v}_2 \in \mathbb{R}^{d/2}$ (a rendezvous burn applied just before \mathbf{x}_f at time t_f), and t_f as our only remaining decision variables. If we conduct a search for $t_f^* \in [t_0, t_0 + T_{\max}]$, the relaxed-2PBVP can now be solved iteratively as a relatively simple bounded one-dimensional nonlinear minimization problem, where at each iteration one computes:

$$\Delta \mathbf{V}^*(t_f) = \Phi_v^{-1}(t_f, \{t_0, t_f\})(\mathbf{x}_f - \Phi(t_f, t_0)\mathbf{x}_0),$$

where the argument t_f is shown for $\Delta \mathbf{V}^*$ to highlight its dependence. By uniqueness of the matrix inverse (provided Φ_v^{-1} is non-singular, discussed below), we need only check that the resulting impulses $\Delta \mathbf{v}_i^*(t_f)$ satisfy the magnitude bound to declare the solution to an iteration feasible. Notice that because Φ and Φ_v^{-1} depend only on the difference between t_f and t_0 , we can equivalently search over various $t_f - t_0 \in [0, T_{\max}]$ instead, using the expression:

$$\Delta \mathbf{V}^*(t_f - t_0) = \Phi_v^{-1}(t_f - t_0, \{0, t_f - t_0\})(\mathbf{x}_f - \Phi(t_f - t_0, 0)\mathbf{x}_0), \quad (14)$$

which reveals that our impulsive steering problem depends only on the maneuver duration $T = t_f - t_0$ (provided \mathbf{x}_f and \mathbf{x}_0 are given). This will be indispensable for precomputation, as it allows steering trajectories to be generated and stored *offline*. Regarding singularities, our steering solution $\Delta \mathbf{V}^* = \arg \min_{t_f}(\Delta \mathbf{V}^*(t_f - t_0))$ requires that Φ_v be invertible, *i.e.*, that $(t_f - \tau_1) - (t_f - \tau_2) = t_f - t_0$ avoids certain values (such as zero and certain values longer than one period [36], including orbital period multiples) which we achieve by restricting T_{\max} to be shorter than one orbital period. To handle $t_f - t_0 = 0$ exactly, note a solution to the 2PBVP exists if and only if \mathbf{x}_0 and \mathbf{x}_f differ in velocity only; in such cases, we take this velocity difference as $\Delta \mathbf{v}_2^*$ (with $\Delta \mathbf{v}_1^* = \mathbf{0}$) to be the solution.

B Reachability Sets

In keeping with Eq. (14), since $\Delta \mathbf{V}^* = \arg \min_T(\Delta \mathbf{V}^*(T))$ only depends on \mathbf{x}_f and \mathbf{x}_0 , we henceforth refer to the cost of a steering trajectory by the notation $J(\mathbf{x}_0, \mathbf{x}_f)$. We then define the forward *reachability set* from a given state \mathbf{x}_0 as follows:

Definition 6 (Forward Reachable Set). The forward reachable set \mathcal{R} from state \mathbf{x}_0 is the set of all states \mathbf{x}_f that can be reached from \mathbf{x}_0 with a cost $J(\mathbf{x}_0, \mathbf{x}_f)$ below a given cost threshold \bar{J} , *i.e.*,

$$\mathcal{R}(\mathbf{x}_0, \bar{J}) \triangleq \{\mathbf{x}_f \in \mathcal{X} \mid J(\mathbf{x}_0, \mathbf{x}_f) < \bar{J}\}.$$

Recall from Eq. (14) in Section IV A that the steering cost may be written as:

$$J(\mathbf{x}_0, \mathbf{x}_f) = \|\Delta \mathbf{v}_1\| + \|\Delta \mathbf{v}_2\| = \|\mathbf{S}_1 \Delta \mathbf{V}\| + \|\mathbf{S}_2 \Delta \mathbf{V}\| \quad (15)$$

where $\mathbf{S}_1 = [\mathbf{I}_{d/2 \times d/2} \ \mathbf{0}_{d/2 \times d/2}]$, $\mathbf{S}_2 = [\mathbf{0}_{d/2 \times d/2} \ \mathbf{I}_{d/2 \times d/2}]$, and $\Delta \mathbf{V}$ is given by:

$$\Delta \mathbf{V}(\mathbf{x}_0, \mathbf{x}_f) = \begin{bmatrix} \Delta \mathbf{v}_1 \\ \Delta \mathbf{v}_2 \end{bmatrix} = \Phi_v^{-1}(t_f, \{t_0, t_f\})(\mathbf{x}_f - \Phi(t_f, t_0)\mathbf{x}_0).$$

The cost function $J(\mathbf{x}_0, \mathbf{x}_f)$ is difficult to gain insight on directly; however, as we shall see, we can work with its bounds much more easily.

Lemma 7 (Fuel Burn Cost Bounds). *For the cost function in Eq. (15), we have the following upper and lower bounds:*

$$\|\Delta \mathbf{V}\| \leq J(\mathbf{x}_0, \mathbf{x}_f) \leq \sqrt{2}\|\Delta \mathbf{V}\|.$$

Proof. For the proof, see Appendix B. □

Now, observe that $\|\Delta \mathbf{V}\| = \sqrt{(\mathbf{x}_f - \Phi(t_f, t_0)\mathbf{x}_0)^T \mathbf{G}^{-1}(\mathbf{x}_f - \Phi(t_f, t_0)\mathbf{x}_0)}$ where $\mathbf{G}^{-1} = \Phi_v^{-T} \Phi_v^{-1}$, *i.e.*, the expression for an ellipsoid $\mathcal{E}(\mathbf{x}_f)$ resolved in the LVLH frame with matrix \mathbf{G}^{-1} and center $\Phi(t_f, t_0)\mathbf{x}_0$ (the state $T = t_f - t_0$ time units ahead of \mathbf{x}_0 along its coasting arc). Combined with Lemma 7, we see that for a fixed maneuver time T and propellant cost threshold \bar{J} , the spacecraft at \mathbf{x}_0 can reach all states inside an area under-approximated by an ellipsoid with matrix $\mathbf{G}^{-1}/\bar{J}^2$ and over-approximated by an ellipsoid of matrix $\sqrt{2}\mathbf{G}^{-1}/\bar{J}^2$. The forward reachable set for impulsive

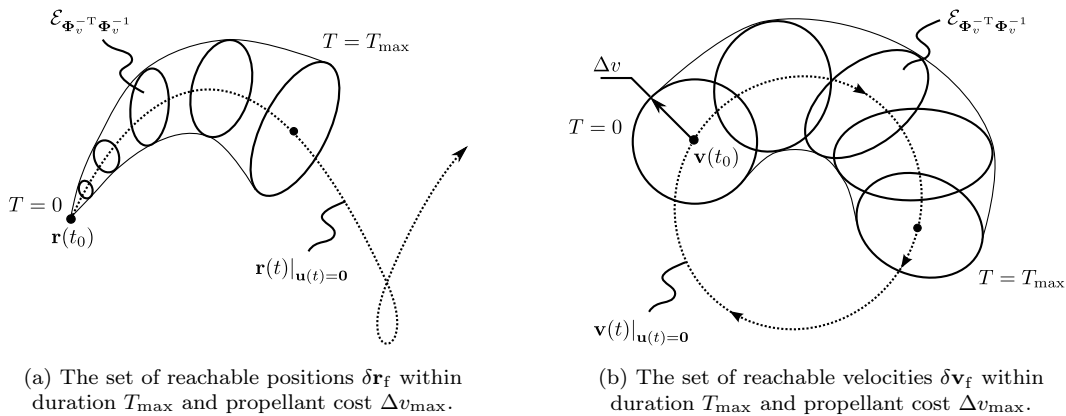


Fig. 5 Bounds on reachability sets from initial state $\mathbf{x}(t_0)$ under propellant cost threshold \bar{J} .

CWH dynamics under the 2-norm metric is therefore bounded by the union over all maneuver times of these under- and over-approximating ellipsoidal sets, respectively. See Fig. 5 for visualization.

C Algorithm

As mentioned in Section I, we apply a modified version of the Fast Marching Tree (FMT*) sampling-based planning algorithm to solve the problem in Eq. (1). Sampling-based planning [15, 37] essentially breaks down a continuous trajectory optimization problem into a series of relaxed, local steering problems (as in Section IV A) between intermediate waypoints (called *samples*) before piecing them together to form a global solution to the original problem. This framework can yield significant computational benefits if: (i) the relaxed subproblems are simple enough, and (ii) the *a posteriori* evaluation of trajectory constraints is fast compared to a single solution of the full-scale problem. Furthermore, provided samples are sufficiently dense in the free state-space $\mathcal{X}_{\text{free}}$ and graph exploration is spatially symmetric, sampling-based planners can closely approximate global optima without fear of convergence to local minima. Though many candidate planners could be used here, we rely on the asymptotically-optimal (AO) FMT* algorithm for its efficiency (see [23] for details on the advantages of FMT* over its state-of-the-art counterparts) and its compatibility with *deterministic* (as opposed to random) sampling sequences [38], which leads to a number of algorithmic simplifications (including use of offline knowledge).

The FMT* algorithm, tailored to our application, is presented as Algorithm 1 (we shall henceforth refer to our modified version of FMT* as simply FMT*, for brevity). FMT* efficiently expands

a tree of feasible trajectories from an initial state \mathbf{x}_{init} to a goal state \mathbf{x}_{goal} around nearby obstacles. It begins by taking a set of samples distributed in the free state space $\mathcal{X}_{\text{free}}$ using the `SAMPLEFREE` routine, which restricts state sampling to actively-safe, collision-free samples (which lie outside of \mathcal{X}_{obs} and have access to a safe Collision-Avoidance Maneuver (CAM) as described in Section III C). In our implementation, we assume samples are taken using a particular deterministic, low-dispersion sequence called the Halton sequence [39], though any deterministic, *low-dispersion* sampling sequence may be used [38]. Selecting \mathbf{x}_{init} first for further expansion as the minimum cost-to-come node \mathbf{z} , the algorithm then proceeds to look at reachable samples or “neighbors” (samples that can be reached with less than a given propellant cost threshold \bar{J} , as described in the previous subsection) and attempts connections (using `STEER`) to those with cheapest cost-to-come back to the tree. The cost threshold \bar{J} is a free parameter whose value can have a significant effect on performance; see Theorem 12 for a theoretical characterization and Section VI for a representative numerical trade study. Those trajectories satisfying the constraints of Eq. (1), as determined by `COLLISIONFREE`, are saved. As feasible connections are made, the algorithm relies on adding and removing nodes (saved waypoint states) from three sets: a set of unexplored samples $\mathcal{V}_{\text{unvisited}}$ not yet connected to the tree, a frontier $\mathcal{V}_{\text{open}}$ of nodes likely to make efficient connections to unexplored neighbors, and an interior $\mathcal{V}_{\text{closed}}$ of nodes that are no longer useful for exploring the state space \mathcal{X} . Details on FMT* can be found in its original work [23].

To make FMT* amenable to a real-time implementation, we consider an online-offline approach that relegates as much computation as possible to a pre-processing phase. To be specific, the sample set \mathcal{S} (line 2), nearest-neighbor sets (used in lines 5 and 6), and steering trajectory solutions (line 7) may be entirely pre-processed, assuming the planning problem satisfies the following conditions:

1. the state space \mathcal{X} is known *a priori*, as is typical for most LEO missions (a luxury we do not generally have for the obstacle space \mathcal{X}_{obs} , which must be identified online using onboard sensors once the spacecraft arrives at \mathcal{X}),
2. steering solutions are independent of sample arrival times t_0 , as we show in Section IV A.

Here Item 1 allows samples to be precomputed, while Item 2 enables steering trajectories to be stored onboard or uplinked from the ground up to the spacecraft, since their values remain relevant

Algorithm 1 The Fast Marching Tree Algorithm (FMT*). Computes a minimal-cost trajectory from an initial state $\mathbf{x}(t_0) = \mathbf{x}_{\text{init}}$ to a target state \mathbf{x}_{goal} through a fixed number n of samples \mathcal{S} .

```

1: Add  $\mathbf{x}_{\text{init}}$  to the root of the tree  $\mathcal{T}$ , as a member of the frontier set  $\mathcal{V}_{\text{open}}$ 
2: Generate samples  $\mathcal{S} \leftarrow \text{SAMPLEFREE}(\mathcal{X}, n, t_0)$  and add them to the unexplored set  $\mathcal{V}_{\text{unvisited}}$ 
3: Set the minimum cost-to-come node in the frontier set as  $\mathbf{z} \leftarrow \mathbf{x}_{\text{init}}$ 
4: while true do
5:   for each neighbor  $\mathbf{x}$  of  $\mathbf{z}$  in  $\mathcal{V}_{\text{unvisited}}$  do
6:     Find the neighbor  $\mathbf{x}_{\text{min}}$  in  $\mathcal{V}_{\text{open}}$  of cheapest cost-to-go to  $\mathbf{x}$ 
7:     Compute the trajectory between them as  $[\mathbf{x}(t), \mathbf{u}(t), t] \leftarrow \text{STEER}(\mathbf{x}_{\text{min}}, \mathbf{x})$  (see Section IVA)
8:     if COLLISIONFREE( $\mathbf{x}(t), \mathbf{u}(t), t$ ) then
9:       Add the trajectory from  $\mathbf{x}_{\text{min}}$  to  $\mathbf{x}$  to tree  $\mathcal{T}$ 
10:    Remove all  $\mathbf{x}$  from the unexplored set  $\mathcal{V}_{\text{unvisited}}$ 
11:    Add any new connections  $\mathbf{x}$  to the frontier  $\mathcal{V}_{\text{open}}$ 
12:    Remove  $\mathbf{z}$  from the frontier  $\mathcal{V}_{\text{open}}$  and add it to  $\mathcal{V}_{\text{closed}}$ 
13:    if  $\mathcal{V}_{\text{open}}$  is empty then
14:      return Failure
15:    Reassign  $\mathbf{z}$  as the node in  $\mathcal{V}_{\text{open}}$  with smallest cost-to-come from the root ( $\mathbf{x}_{\text{init}}$ )
16:    if  $\mathbf{z}$  is in the goal region  $\mathcal{X}_{\text{goal}}$  then
17:      return Success, and the unique trajectory from the root ( $\mathbf{x}_{\text{init}}$ ) to  $\mathbf{z}$ 

```

regardless of the times at which the spacecraft actually follows them during the mission. This leaves only collision-checking, graph construction, and termination checks as parts of the online phase, greatly improving the online run time and leaving the more intensive work to offline resources where running time is less important. This breakdown into online and offline components (inspired by [40]) is a valuable technique for imbuing kinodynamic motion planning problems with real-time online solvability using fast batch-planners like FMT*.

D Theoretical Characterization

It remains to show that FMT* provides similar asymptotic optimality and convergence rate guarantees under the 2-norm propellant-cost metric and impulsive CWH dynamics (which enter into Algorithm 1 under lines 6–7), as it does for kinematic (straight-line path planning) problems [23]. For sampling-based algorithms, *asymptotic optimality* refers to the property that as the number of samples $n \rightarrow \infty$, the cost of the trajectory (a.k.a. “path”) returned by the planner approaches that of the optimal cost. Here a proof is presented showing asymptotic optimality for the planning algorithm and problem setup used in this paper. We note that while CWH dynamics are the primary focus of this work, the following proof methodology extends to any general linear system controlled by a finite sequence of impulsive actuations, whose fixed-duration 2-impulse steering problem is uniquely determined (*e.g.*, a wide array of second-order control systems).

The proof proceeds analogously to [23] by showing that it is always possible to construct an approximate path from points in \mathcal{S} that closely follows the optimal path. Similarly to [23], we will make use here of a concept called the ℓ_2 -dispersion of a set of points, which upper bounds how far away a point in \mathcal{X} can be from its nearest point in \mathcal{S} as measured by the ℓ_2 -norm.

Definition 8 (ℓ_2 -dispersion). For a finite, non-empty set \mathcal{S} of points in a d -dimensional compact Euclidean subspace \mathcal{X} with positive Lebesgue measure, its ℓ_2 -dispersion $D(\mathcal{S})$ is defined as:

$$\begin{aligned} D(\mathcal{S}) &\triangleq \sup_{\mathbf{x} \in \mathcal{X}} \min_{\mathbf{s} \in \mathcal{S}} \|\mathbf{s} - \mathbf{x}\| \\ &= \sup\{R > 0 \mid \exists \mathbf{x} \in \mathcal{X} \text{ with } \mathcal{B}(\mathbf{x}, R) \cap \mathcal{S} = \emptyset\}, \end{aligned}$$

where $\mathcal{B}(\mathbf{x}, R)$ is a Euclidean ball with radius R centered at state \mathbf{x} .

We also require a means for quantifying the deviation that small endpoint perturbations can bring about in the 2-impulse steering control. This result is necessary to ensure that the particular placement of the points of \mathcal{S} is immaterial; only its low-dispersion property matters.

Lemma 9 (Steering with Perturbed Endpoints). *For a given steering trajectory $\mathbf{x}(t)$ with initial time t_0 and final time t_f , let $\mathbf{x}_0 := \mathbf{x}(t_0)$, $\mathbf{x}_f := \mathbf{x}(t_f)$, $T := t_f - t_0$, and $J := J(\mathbf{x}_0, \mathbf{x}_f)$. Consider now the steering trajectory $\tilde{\mathbf{x}}(t)$ between perturbed start and end points $\tilde{\mathbf{x}}_0 = \mathbf{x}_0 + \delta\mathbf{x}_0$ and $\tilde{\mathbf{x}}_f = \mathbf{x}_f + \delta\mathbf{x}_f$.*

Case 1: $T = 0$. *There exists a perturbation center $\delta\mathbf{x}_c$ (consisting of only a position shift) with $\|\delta\mathbf{x}_c\| = \mathcal{O}(J^2)$ such that if $\|\delta\mathbf{x}_0\| \leq \eta J^3$ and $\|\delta\mathbf{x}_f - \delta\mathbf{x}_c\| \leq \eta J^3$ then $J(\tilde{\mathbf{x}}_0, \tilde{\mathbf{x}}_f) \leq J(1 + 4\eta + \mathcal{O}(J))$ and the spatial deviation of the perturbed trajectory from $\mathbf{x}(t)$ is $\mathcal{O}(J)$.*

Case 2: $T > 0$. *If $\|\delta\mathbf{x}_0\| \leq \eta J^3$ and $\|\delta\mathbf{x}_f\| \leq \eta J^3$ then $J(\tilde{\mathbf{x}}_0, \tilde{\mathbf{x}}_f) \leq J(1 + \mathcal{O}(\eta J^2 T^{-1}))$ and the spatial deviation of the perturbed trajectory from $\mathbf{x}(t)$ is $\mathcal{O}(J)$.*

Proof. For the proof, see Appendix B. □

We are now in a position to prove that the cost of the trajectory returned by FMT* approaches that of an optimal trajectory as the number of samples $n \rightarrow \infty$. The proof proceeds in two steps. First, we establish that there is a sequence of waypoints in \mathcal{S} that are placed closely along the optimal path and approximately evenly-spaced in cost. Then we show that the existence of these

waypoints guarantees that FMT* finds a path with a cost close to that of the optimal cost. The theorem and proof combine elements from Theorem 1 in [23] and Theorem IV.6 from [41].

Definition 10 (Strong δ -Clearance). A trajectory $\mathbf{x}(t)$ is said to have *strong* δ -clearance if, for some $\delta > 0$ and all t , the Euclidean distance between $\mathbf{x}(t)$ and any point in \mathcal{X}_{obs} is greater than δ .

Theorem 11 (Existence of Waypoints near an Optimal Path). *Let $\mathbf{x}^*(t)$ be a feasible trajectory for the motion planning problem Eq. (1) with strong δ -clearance, let $\mathbf{u}^*(t) = \sum_{i=1}^N \Delta \mathbf{v}_i^* \cdot \delta(t - \tau_i^*)$ be its associated control trajectory, and let J^* be its cost. Furthermore, let $\mathcal{S} \cup \{\mathbf{x}_{\text{init}}\}$ be a set of $n \in \mathbb{N}$ points from $\mathcal{X}_{\text{free}}$ with dispersion $D(\mathcal{S}) \leq \gamma n^{-1/d}$. Let $\epsilon > 0$, and choose $\bar{J} = 4(\gamma n^{-1/d} / \epsilon)^{1/3}$. Then, provided that n is sufficiently large, there exists a sequence of points $\{\mathbf{y}_k\}_{k=0}^K$, $\mathbf{y}_k \in \mathcal{S}$ such that $J(\mathbf{y}_k, \mathbf{y}_{k+1}) \leq \bar{J}$, the cost of the path $\mathbf{y}(t)$ made by joining all of the steering trajectories between \mathbf{y}_k and \mathbf{y}_{k+1} is $\sum_{k=0}^{K-1} J(\mathbf{y}_k, \mathbf{y}_{k+1}) \leq (1 + \epsilon)J^*$, and $\mathbf{y}(t)$ is itself strong $(\delta/2)$ -clear.*

Proof. We first note that if $J^* = 0$ then we can pick $\mathbf{y}_0 = \mathbf{x}^*(t_0)$ and $\mathbf{y}_1 = \mathbf{x}^*(t_f)$ as the only points in $\{\mathbf{y}_k\}$ and the result is trivial. Thus assume that $J^* > 0$. Construct a sequence of times $\{t_k\}_{k=0}^K$ and corresponding points $\mathbf{x}_k^* = \mathbf{x}^*(t_k)$ spaced along $\mathbf{x}^*(t)$ in cost intervals of $\bar{J}/2$. We admit a slight abuse of notation here in that $\mathbf{x}^*(\tau_i^*)$ may represent a state with any velocity along the length of the impulse $\Delta \mathbf{v}_i^*$; to be precise, pick $\mathbf{x}_0^* = \mathbf{x}_{\text{init}}$, $t_0 = 0$, and for $k = 1, 2, \dots$ define $j_k = \min\left\{j \mid \sum_{i=1}^j \|\Delta \mathbf{v}_i^*\| > k \frac{\bar{J}}{2}\right\}$ and select t_k and \mathbf{x}_k^* as:

$$t_k = \tau_{j_k}^*$$

$$\mathbf{x}_k^* = \lim_{t \rightarrow t_k^-} \mathbf{x}^*(t) + \left(k \frac{\bar{J}}{2} - \sum_{i=1}^{j_k-1} \|\Delta \mathbf{v}_i^*\| \right) \mathbf{B} \frac{\Delta \mathbf{v}_{j_k}^*}{\|\Delta \mathbf{v}_{j_k}^*\|}.$$

Let $K = \lceil J^* \rceil / (\bar{J}/2)$ and set $t_K = t_f$, $\mathbf{x}_K^* = \mathbf{x}^*(t_f)$. Since the trajectory $\mathbf{x}^*(t)$ to be approximated is fixed, for sufficiently small \bar{J} (equivalently, sufficiently large n) we may ensure that the control applied between each \mathbf{x}_k^* and \mathbf{x}_{k+1}^* occurs only at the endpoints. In particular this may be accomplished by choosing n large enough so that $\bar{J} < \min_i \|\Delta \mathbf{v}_i^*\|$. In the limit $\bar{J} \rightarrow 0$, the vast majority of the 2-impulse steering connections between successive \mathbf{x}_k^* will be zero-time maneuvers (arranged along the length of each burn $\Delta \mathbf{v}_i^*$) with only N positive-time maneuvers spanning the regions of

$\mathbf{x}^*(t)$ between burns. By considering this regime of n , we note that applying 2-impulse steering between successive \mathbf{x}_k^* (which otherwise may only approximate the performance of a more complex control scheme) requires cost no greater than that of \mathbf{x}^* itself along that step, *i.e.*, $\bar{J}/2$.

We now inductively define a sequence of points $\{\hat{\mathbf{x}}_k^*\}_{k=0}^K$ by $\hat{\mathbf{x}}_0^* = \mathbf{x}_0^*$ and for each $k > 0$: (1) if $t_k = t_{k-1}$, pick $\hat{\mathbf{x}}_k^* = \mathbf{x}_k^* + \delta\mathbf{x}_{c,k} + (\hat{\mathbf{x}}_{k-1}^* - \mathbf{x}_{k-1}^*)$, where $\delta\mathbf{x}_{c,k}$ comes from Lemma 9 for zero-time approximate steering between \mathbf{x}_{k-1}^* and \mathbf{x}_k^* subject to perturbations of size ϵJ^3 ; (2) otherwise if $t_k > t_{k-1}$, pick $\hat{\mathbf{x}}_k^* = \mathbf{x}_k^* + (\hat{\mathbf{x}}_{k-1}^* - \mathbf{x}_{k-1}^*)$. The reason for defining these $\hat{\mathbf{x}}_k^*$ is that the process of approximating each $\Delta\mathbf{v}_i^*$ by a sequence of small burns necessarily incurs some short-term position drift. Since $\delta\mathbf{x}_{c,k} = O(\bar{J}^2)$ for each k , and since $K = O(\bar{J}^{-1})$, the maximum accumulated difference satisfies $\max_k \|\hat{\mathbf{x}}_k^* - \mathbf{x}_k^*\| = O(\bar{J})$.

For each k consider the Euclidean ball centered at $\hat{\mathbf{x}}_k^*$ with radius $\gamma n^{-\frac{1}{d}}$, *i.e.*, let $\mathcal{B}_k := \mathcal{B}(\hat{\mathbf{x}}_k^*, \gamma n^{-\frac{1}{d}})$. By Definition 8 and our restriction on \mathcal{S} , each \mathcal{B}_k contains at least one point from \mathcal{S} . Hence for every \mathcal{B}_k we can pick a waypoint \mathbf{y}_k such that $\mathbf{y}_k \in \mathcal{B}_k \cap \mathcal{S}$. Then $\|\mathbf{y}_k - \hat{\mathbf{x}}_k^*\| \leq \gamma n^{-\frac{1}{d}} = \epsilon(\bar{J}/2)^3/8$ for all k , and thus by Lemma 9 (with $\eta = \epsilon/8$) we have that:

$$J(\mathbf{y}_k, \mathbf{y}_{k+1}) \leq \frac{\bar{J}}{2} \left(1 + \frac{\epsilon}{2} + O(\bar{J}) \right) \leq \frac{\bar{J}}{2} (1 + \epsilon)$$

for sufficiently large n . In applying Lemma 9 to Case 2 for k such that $t_{k+1} > t_k$, we note that the T^{-1} term is mitigated by the fact that there are only a finite number of burn times τ_i^* along $\mathbf{x}^*(t)$. Thus for each such k , $t_{k+1} - t_k \geq \min_j (t_{j+1} - t_j) > 0$, so in every case we have $J(\mathbf{y}_k, \mathbf{y}_{k+1}) \leq (\bar{J}/2)(1 + \epsilon)$. That is, each steering segment connecting \mathbf{y}_k to \mathbf{y}_{k+1} approximates the cost of the corresponding \mathbf{x}_k^* to \mathbf{x}_{k+1}^* segment of $\mathbf{x}^*(t)$ up to a multiplicative factor of ϵ , and thus:

$$\sum_{k=0}^{K-1} J(\mathbf{y}_k, \mathbf{y}_{k+1}) \leq (1 + \epsilon) J^*.$$

Finally, to establish that $\mathbf{y}(t)$, the trajectory formed by steering through the \mathbf{y}_k 's in succession, has sufficient obstacle clearance, we note that its distance from $\mathbf{x}^*(t)$ is bounded by $\max_k \|\hat{\mathbf{x}}_k^* - \mathbf{x}_k^*\| = O(\bar{J})$ plus the deviation bound from Definition 8, again $O(\bar{J})$. For sufficiently large n , the total distance, $O(\bar{J})$, will be bounded by $\delta/2$, and thus $\mathbf{y}(t)$ will have strong $(\delta/2)$ -clearance. \square

We now prove that FMT* is asymptotically optimal in the number of points n , provided the conditions required in Theorem 11 hold; note the proof is heavily based on Theorem VI.1 from [42].

Theorem 12 (Asymptotic Performance of FMT*). *Let $\mathbf{x}^*(t)$ be a feasible trajectory satisfying Eq. (1) with strong δ -clearance and cost J^* . Let $\mathcal{S} \cup \{\mathbf{x}_0\}$ be a set of $n \in \mathbb{N}$ samples from $\mathcal{X}_{\text{free}}$ with dispersion $D(\mathcal{S}) \leq \gamma n^{-1/d}$. Finally, let J_n denote the cost of the path returned by FMT* with n points in \mathcal{S} while using a cost threshold $\bar{J}(n) = \omega(n^{-1/3d})$ and $\bar{J} = o(1)$. (That is, $\bar{J}(n)$ asymptotically dominates $n^{-1/3d}$ and is asymptotically dominated by 1.) Then $\lim_{n \rightarrow \infty} J_n \leq J^*$.*

Proof. Let $\epsilon > 0$. Pick n sufficiently large so that $\delta/2 \geq \bar{J} \geq 4(\gamma n^{-1/d}/\epsilon)^{1/3}$ such that Theorem 11 holds. That is, there exists a sequence of waypoints $\{\mathbf{y}_k\}_{k=0}^K$ approximating $\mathbf{x}^*(t)$ such that the trajectory $\mathbf{y}(t)$ created by sequentially steering through the \mathbf{y}_k is strong $\delta/2$ -clear, whose connection costs satisfy $J(\mathbf{y}_k, \mathbf{y}_{k+1}) \leq \bar{J}$, and whose total cost satisfies $\sum_{k=0}^{K-1} J(\mathbf{y}_k, \mathbf{y}_{k+1}) \leq (1+\epsilon)J^*$. We show that FMT* recovers a path with cost at least as good as $\mathbf{y}(t)$; that is, we show that $\lim_{n \rightarrow \infty} J_n \leq J^*$.

Consider running FMT* to completion, and for each \mathbf{y}_k , let $c(\mathbf{y}_k)$ denote the cost-to-come of \mathbf{y}_k in the generated graph (with value ∞ if \mathbf{y}_k is not connected). We show by induction that:

$$\min(c(\mathbf{y}_m), J_n) \leq \sum_{k=0}^{m-1} J(\mathbf{y}_k, \mathbf{y}_{k+1}) \quad (16)$$

for all $m \in [1, \dots, K]$. For the base case $m = 1$, we note by the initialization of FMT* on line 1 of Algorithm 1 that \mathbf{x}_{init} is in $\mathcal{V}_{\text{open}}$; therefore, by the design of FMT* (per lines 5–9), every possible feasible connection is made between the first waypoint $\mathbf{y}_0 = \mathbf{x}_{\text{init}}$ and its neighbors. Since $J(\mathbf{y}_0, \mathbf{y}_1) \leq \bar{J}$ and the edge $(\mathbf{y}_0, \mathbf{y}_1)$ is collision free, it is also in the FMT* graph. Then $c(\mathbf{y}_1) = J(\mathbf{y}_0, \mathbf{y}_1)$. Now assuming that Eq. (16) holds for $m - 1$, then one of the following statements holds:

1. $J_n \leq \sum_{k=0}^{m-2} J(\mathbf{y}_k, \mathbf{y}_{k+1})$
2. $c(\mathbf{y}_{m-1}) \leq \sum_{k=0}^{m-2} J(\mathbf{y}_k, \mathbf{y}_{k+1})$ and FMT* ends before considering \mathbf{y}_m .
3. $c(\mathbf{y}_{m-1}) \leq \sum_{k=0}^{m-2} J(\mathbf{y}_k, \mathbf{y}_{k+1})$ and $\mathbf{y}_{m-1} \in \mathcal{V}_{\text{open}}$ when \mathbf{y}_m is first considered
4. $c(\mathbf{y}_{m-1}) \leq \sum_{k=0}^{m-2} J(\mathbf{y}_k, \mathbf{y}_{k+1})$ and $\mathbf{y}_{m-1} \notin \mathcal{V}_{\text{open}}$ when \mathbf{y}_m is first considered.

We now show for each case that our inductive hypothesis holds.

Case 1: $J_n \leq \sum_{k=0}^{m-2} J(\mathbf{y}_k, \mathbf{y}_{k+1}) \leq \sum_{k=0}^{m-1} J(\mathbf{y}_k, \mathbf{y}_{k+1})$.

Case 2: Since at every step FMT* considers the node that is the endpoint of the path with the lowest cost, if FMT* ends before considering \mathbf{y}_m , we have $J_n \leq c(\mathbf{y}_m) \leq c(\mathbf{y}_{m-1}) + J(\mathbf{y}_{m-1}, \mathbf{y}_m) \leq \sum_{k=0}^{m-1} J(\mathbf{y}_k, \mathbf{y}_{k+1})$.

Case 3: Since the neighborhood of \mathbf{y}_m is collision free by the clearance property of \mathbf{y} , and since \mathbf{y}_{m-1} is a possible parent candidate for connection, \mathbf{y}_m will be added to the FMT* tree as soon as it is considered with $c(\mathbf{y}_m) \leq c(\mathbf{y}_{m-1}) + J(\mathbf{y}_{m-1}, \mathbf{y}_m) \leq \sum_{k=0}^{m-1} J(\mathbf{y}_k, \mathbf{y}_{k+1})$.

Case 4: When \mathbf{y}_m is considered, it means there is a node $\mathbf{z} \in \mathcal{V}_{\text{open}}$ (with minimum cost-to-come through the FMT* tree) and $\mathbf{y}_m \in \mathcal{R}(\mathbf{z}, \bar{J})$. Then $c(\mathbf{y}_m) \leq c(\mathbf{z}) + J(\mathbf{z}, \mathbf{y}_m)$. Since $c(\mathbf{y}_{m-1}) < \infty$, \mathbf{y}_{m-1} must be added to the tree by the time FMT* terminates. Consider the path from \mathbf{x}_{init} to \mathbf{y}_{m-1} in the final FMT* tree, and let \mathbf{w} be the last vertex along this path, which is in $\mathcal{V}_{\text{open}}$ at the time when \mathbf{y}_m is considered. If $\mathbf{y}_m \in \mathcal{R}(\mathbf{w}, \bar{J})$, *i.e.*, \mathbf{w} is a parent candidate for connection, then:

$$\begin{aligned} c(\mathbf{y}_m) &\leq c(\mathbf{w}) + J(\mathbf{w}, \mathbf{y}_m) \\ &\leq c(\mathbf{w}) + J(\mathbf{w}, \mathbf{y}_{m-1}) + J(\mathbf{y}_{m-1}, \mathbf{y}_m) \\ &\leq c(\mathbf{y}_{m-1}) + J(\mathbf{y}_{m-1}, \mathbf{y}_m) \\ &\leq \sum_{k=0}^{m-1} J(\mathbf{y}_k, \mathbf{y}_{k+1}). \end{aligned}$$

Otherwise if $\mathbf{y}_m \notin \mathcal{R}(\mathbf{w}, \bar{J})$, then $J(\mathbf{w}, \mathbf{y}_m) > \bar{J}$ and:

$$\begin{aligned} c(\mathbf{y}_m) &\leq c(\mathbf{z}) + J(\mathbf{z}, \mathbf{y}_m) \\ &\leq c(\mathbf{w}) + \bar{J} \\ &\leq c(\mathbf{w}) + J(\mathbf{w}, \mathbf{y}_m) \\ &\leq c(\mathbf{w}) + J(\mathbf{w}, \mathbf{y}_{m-1}) + J(\mathbf{y}_{m-1}, \mathbf{y}_m) \\ &\leq c(\mathbf{y}_{m-1}) + J(\mathbf{y}_{m-1}, \mathbf{y}_m) \\ &\leq \sum_{k=0}^{m-1} J(\mathbf{y}_k, \mathbf{y}_{k+1}). \end{aligned}$$

where we used the fact that \mathbf{w} is on the path of \mathbf{y}_{m-1} to establish $c(\mathbf{w}) + J(\mathbf{w}, \mathbf{y}_{m-1}) \leq c(\mathbf{y}_{m-1})$.

Thus by induction Eq. (16) holds for all m . Taking $m = K$, we finally have that $J_n \leq c(\mathbf{y}_K) \leq \sum_{k=0}^{K-1} J(\mathbf{y}_k, \mathbf{y}_{k+1}) \leq (1 + \epsilon)J^*$, as desired. \square

Remark 13 (Asymptotic Optimality of FMT*). If the planning problem at hand admits an optimal solution that does not itself have strong δ -clearance, but is arbitrarily approximable both pointwise and in cost by trajectories with strong clearance (see [42] for additional discussion on why such an assumption is reasonable), then Theorem 12 implies the asymptotic optimality of FMT*.

V Trajectory Smoothing

Due to the discreteness caused by using a *finite* number of samples, sampling-based solutions will necessarily be approximations to true optima. In an effort to compensate for this limitation, we offer in this section two techniques to improve the quality of solutions returned by our planner from Section IV C. We first describe a straightforward method for reducing the sum of Δv -vector magnitudes along concatenated sequences of edge trajectories that can also be used to improve the search for propellant-efficient trajectories in the feasible state space $\mathcal{X}_{\text{free}}$. We then follow with a fast post-processing algorithm for further reducing propellant cost after a solution has been reported.

The first technique removes unnecessary Δv -vectors that occur when joining sub-trajectories (edges) in the planning graph. Consider merging two edges at a node with position $\delta\mathbf{r}(t)$ and velocity $\delta\mathbf{v}(t)$ as in Fig. 6a. A naive concatenation would retain both $\Delta\mathbf{v}_2(t^-)$ (the rendezvous burn added to the incoming velocity $\mathbf{v}(t^-)$) and $\Delta\mathbf{v}_1(t)$ (the intercept burn used to achieve the outgoing velocity $\mathbf{v}(t^+)$) individually within the combined control trajectory. Yet, because these impulses occur at the same time, a more realistic approach should merge them into a single net Δv -vector $\Delta\mathbf{v}_{\text{net}}(t^-)$. By the triangle inequality, we have that:

$$\|\Delta\mathbf{v}_{\text{net}}(t^-)\| = \|\Delta\mathbf{v}_2(t^-) + \Delta\mathbf{v}_1(t)\| \leq \|\Delta\mathbf{v}_2(t^-)\| + \|\Delta\mathbf{v}_1(t)\|.$$

Hence, merging edges in this way guarantees Δv savings for solution trajectories under the 2-norm propellant metric. Furthermore, incorporating net Δv 's into the cost-to-come during graph construction can make exploration of the search space more efficient; the cost-to-come $c(\mathbf{z})$ for a given

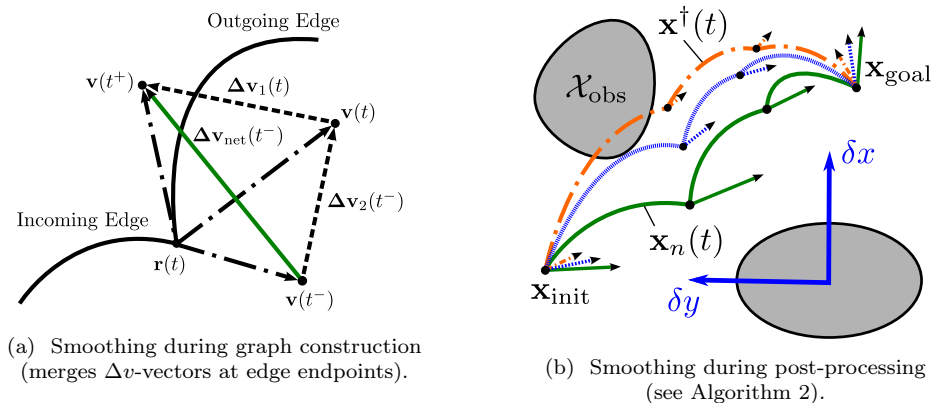


Fig. 6 Improving sampling-based solutions under minimal-propellant impulsive dynamics.

node \mathbf{z} would then reflect the cost to rendezvous with \mathbf{z} from \mathbf{x}_{init} through a series of intermediate intercepts rather than a series of rendezvous maneuvers (as a trajectory designer might normally expect). Note, on the other hand, that two edges as in Fig. 6a that are merged in this fashion no longer achieve velocity $\mathbf{v}(t)$; state $\mathbf{x}(t)$ is skipped altogether. This can be problematic for our active safety policy from Section III C for states along the incoming edge which relies on rendezvousing with the endpoint $\mathbf{x} = [\mathbf{r}(t) \ \mathbf{v}(t)]$ *exactly* before executing our one-burn escape maneuver. To compensate for this, care must be taken to ensure that the burn $\Delta \mathbf{v}_2(t^-)$ that is eliminated during merging is appropriately appended to the front of the escape control trajectory and verified for all possible failure configurations. Hence we see the price of smoothing in this way is that our original one-burn policy now requires an extra burn, which may not be desirable in some applications.

The second technique attempts to reduce solution cost by adjusting the magnitudes of Δv -vectors in the trajectory returned by FMT*, denoted by $\mathbf{x}_n(t)$ with associated stacked impulse vector $\Delta \mathbf{V}_n$. By relaxing FMT*'s constraint to pass through state samples, strong cost improvements may be gained. The main idea is to deform our low-cost, feasible solution $\mathbf{x}_n(t)$ as much as possible towards the unconstrained minimum-propellant solution $\mathbf{x}^*(t)$ between \mathbf{x}_{init} and \mathbf{x}_{goal} , as determined by the 2-point Boundary Value Problem (Eq. (13)) solution from Section IV A (in other words, use a homotopic transformation from $\mathbf{x}_n(t)$ to $\mathbf{x}^*(t)$). However, a naive attempt to solve Eq. (13) in its full generality would be too time-consuming to be useful, and would threaten the real-time capability of our approach. Assuming our sampling-based trajectory is near-optimal (or at least, in a low-cost solution homotopy), we can relax Eq. (13) by keeping the number of burns N , end time $t_f := t_{\text{final}}$,

and burn times τ_i fixed from our planning solution, and solve for an approximate unconstrained minimum-propellant solution $\Delta \mathbf{V}^\dagger$ with associated state trajectory $\mathbf{x}^\dagger(t)$ via:

$$\begin{aligned}
& \underset{\Delta \mathbf{v}_i}{\text{minimize}} && \sum_{i=1}^N \|\Delta \mathbf{v}_i\|_2 \\
& \text{subject to} && \Phi_v(t_{\text{final}}, \{\tau_i\}_i) \Delta \mathbf{V} = \mathbf{x}_{\text{goal}} - \Phi(t_{\text{final}}, t_{\text{init}}) \mathbf{x}_{\text{init}} && \text{Dynamics/Boundary Conditions} \\
& && \|\Delta \mathbf{v}_i\|_2 \leq \Delta v_{\text{max}} \quad \text{for all burns } i && \text{Burn Magnitude Bounds}
\end{aligned} \tag{17}$$

(see Section II C for definitions). It can be shown that Eq. (17) is a second-order cone program (SOCP), and hence quickly solved using standard convex solvers. As the following proof shows explicitly, we can safely deform the trajectory $\mathbf{x}_n(t)$ towards $\mathbf{x}^\dagger(t)$ without violating our dynamics and boundary conditions if we use a convex combination of our two control trajectories $\Delta \mathbf{V}_n$ and $\Delta \mathbf{V}^\dagger$. This follows from the principle of superposition, given that the CWH equations are Linear, Time-Invariant (LTI), and the fact that both solutions already satisfy the boundary conditions.

Theorem 14 (Dynamic Feasibility of CWH Trajectory Smoothing). *Suppose $\mathbf{x}_n(t)$ and $\mathbf{x}^\dagger(t)$ with respective control vectors $\Delta \mathbf{V}_n$ and $\Delta \mathbf{V}^\dagger$ are two state trajectories which satisfy the impulsive CWH steering problem Eq. (12) between states \mathbf{x}_{init} and \mathbf{x}_{goal} . Then the trajectory $\mathbf{x}(t)$ generated by the convex combination of $\Delta \mathbf{V}_n$ and $\Delta \mathbf{V}^\dagger$ is itself a convex combination of $\mathbf{x}_n(t)$ and $\mathbf{x}^\dagger(t)$, and hence also satisfies Eq. (12).*

Proof. Let $\Delta \mathbf{V} = \alpha \Delta \mathbf{V}_n + (1 - \alpha) \Delta \mathbf{V}^\dagger$ for some value $\alpha \in [0, 1]$. From our dynamics equation,

$$\begin{aligned}
\mathbf{x}(t) &= \Phi(t, t_{\text{init}}) \mathbf{x}_{\text{init}} + \Phi_v(t, \{\tau_i\}_i) \Delta \mathbf{V} \\
&= [\alpha + (1 - \alpha)] \Phi(t, t_{\text{init}}) \mathbf{x}_{\text{init}} + \Phi_v(t, \{\tau_i\}_i) [\alpha \Delta \mathbf{V}_n + (1 - \alpha) \Delta \mathbf{V}^\dagger] \\
&= \alpha [\Phi(t, t_{\text{init}}) \mathbf{x}_{\text{init}} + \Phi_v(t, \{\tau_i\}_i) \Delta \mathbf{V}_n] + (1 - \alpha) [\Phi(t, t_{\text{init}}) \mathbf{x}_0 + \Phi_v(t, \{\tau_i\}_i) \Delta \mathbf{V}^\dagger] \\
&= \alpha \mathbf{x}_n(t) + (1 - \alpha) \mathbf{x}^\dagger(t)
\end{aligned}$$

which is a convex combination, as required. Substituting $t = t_{\text{init}}$ or $t = t_{\text{goal}}$, we see that $\mathbf{x}(t)$ satisfies the boundary conditions given that $\mathbf{x}_n(t)$ and $\mathbf{x}^\dagger(t)$ do. This completes the proof. \square

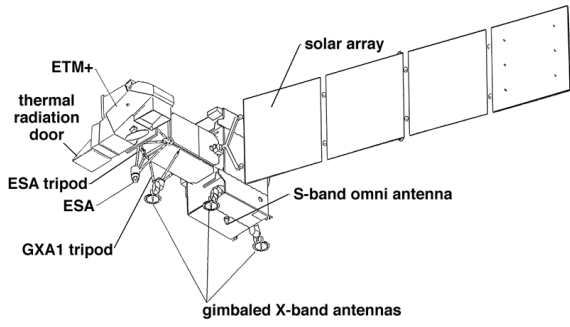
Algorithm 2 “Trajectory smoothing” algorithm for impulsive CWH dynamics. Given a trajectory $\mathbf{x}_n(t)$, $t \in [t_{\text{init}}, t_{\text{goal}}]$ between initial and goal states \mathbf{x}_{init} and \mathbf{x}_{goal} satisfying Eq. (1) with impulses $\Delta \mathbf{V}_n$ applied at times $\{\tau_i\}_i$, returns another feasible trajectory with reduced 2-norm propellant-cost.

- 1: Initialize the smoothed trajectory $\mathbf{x}_{\text{smooth}}(t)$ as $\mathbf{x}_n(t)$, with $\Delta \mathbf{V}_{\text{smooth}} = \Delta \mathbf{V}_n$
 - 2: Compute the unconstrained optimal control vector $\Delta \mathbf{V}^\dagger$ by solving Eq. (17)
 - 3: Compute the unconstrained optimal state trajectory $\mathbf{x}^\dagger(t)$ using Eq. (5) (*See Section IIC*)
 - 4: Initialize weight α and its lower and upper bounds as $\alpha \leftarrow 1$, $\alpha_\ell \leftarrow 0$, $\alpha_u \leftarrow 1$
 - 5: **while** true **do**
 - 6: $\mathbf{x}(t) \leftarrow (1 - \alpha)\mathbf{x}_n(t) + \alpha\mathbf{x}^\dagger(t)$
 - 7: $\Delta \mathbf{V} \leftarrow (1 - \alpha)\Delta \mathbf{V}_n + \alpha\Delta \mathbf{V}^\dagger$
 - 8: **if** COLLISIONFREE($\mathbf{x}(t)$, $\Delta \mathbf{V}$, t) **then**
 - 9: $\alpha_\ell \leftarrow \alpha$
 - 10: Save the smoothed trajectory $\mathbf{x}_{\text{smooth}}(t)$ as $\mathbf{x}(t)$ and control $\Delta \mathbf{V}_{\text{smooth}}$ as $\Delta \mathbf{V}$
 - 11: **else**
 - 12: $\alpha_u \leftarrow \alpha$
 - 13: **if** $\alpha_u - \alpha_\ell$ is less than tolerance $\delta\alpha_{\text{min}} \in (0, 1)$ **then**
 - 14: **break**
 - 15: $\alpha \leftarrow (\alpha_\ell + \alpha_u)/2$
 - 16: **return** the smoothed trajectory $\mathbf{x}_{\text{smooth}}(t)$, with $\Delta \mathbf{V}_{\text{smooth}}$
-

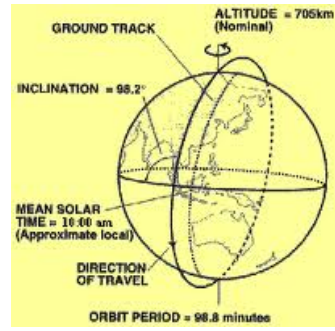
We take advantage of this fact for trajectory-smoothing. Our algorithm, reported as Algorithm 2 and illustrated in Fig. 6b, computes the approximate unconstrained minimum-propellant solution $\mathbf{x}^\dagger(t)$ and returns it (if feasible) or otherwise conducts a bisection line search on α , returning a convex combination of our original planning solution $\mathbf{x}_n(t)$ and $\mathbf{x}^\dagger(t)$ that comes as close to $\mathbf{x}^\dagger(t)$ as possible without violating trajectory constraints. Note because $\Delta \mathbf{V}_n$ lies in the feasible set of Eq. (17), the algorithm can only improve the final propellant cost. By design, Algorithm 2 is geared towards reducing our original solution propellant-cost as quickly as possible while maintaining feasibility; the most expensive computational components are the calculation of $\Delta \mathbf{V}^\dagger$ and collision-checking (consistent with our sampling-based algorithm). Fortunately, the number of collision-checks is limited by the maximum number of iterations $\left\lceil \log_2 \left(\frac{1}{\delta\alpha_{\text{min}}} \right) \right\rceil + 1$, given tolerance $\delta\alpha_{\text{min}} \in (0, 1)$. As an added bonus, for strictly time-constrained applications that require a solution in a fixed amount of time, the algorithm can be easily modified to return the α_ℓ -weighted trajectory $\mathbf{x}_{\text{smooth}}(t)$ when time runs out, as the feasibility of this trajectory is maintained as an algorithm invariant.

VI Numerical Experiments

Consider the two scenarios shown in Fig. 8, here modeling near-field approaches of a chaser spacecraft in close proximity [43] to a target moving in a circular LEO trajectory (as in Fig. 1). We

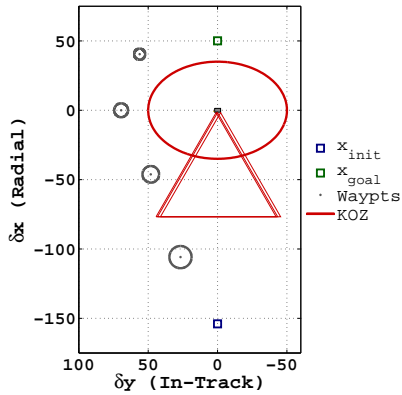


(a) Landsat-7 schematic (Nadir ($-\delta x$ direction) points down, while the in-track ($+\delta y$) direction points left).

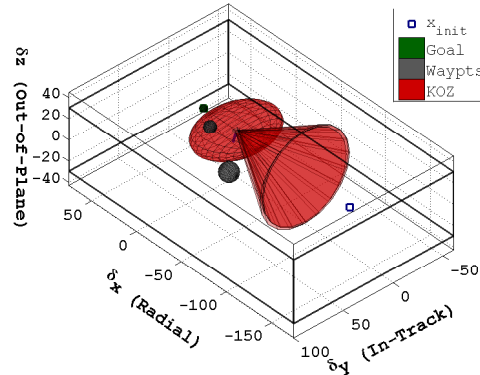


(b) Landsat-7 orbit (Courtesy of the Landsat-7 Handbook).

Fig. 7 Target spacecraft geometry and orbital scenario used in numerical experiments.



(a) Planar motion planning query



(b) 3-dimensional motion planning query.

Fig. 8 Illustrations of the planar and 3D motion plan queries in the LVLH frame.

imagine the chaser, which starts in a circular orbit of lower radius, must be repositioned through a sequence of pre-specified CWH waypoints (*e.g.*, required for equipment checks, surveying, *etc.*) to a coplanar position located radially above the target, arriving with zero relative velocity in preparation for a final radial (“R-bar”) approach. Throughout the maneuver, as described in detail in Section II, the chaser must avoid entering the elliptic target KOZ, enforce hard safety constraints with regard to a two-fault tolerance to stuck-off thruster failures, and otherwise avoid interfering with the target. This includes avoiding the target’s nadir-pointing communication lobes (represented by truncated half-cones), and preventing exhaust plume impingement on its surfaces. For context, we use the Landsat-7 spacecraft and orbit as a reference [44, 3.2] (see Fig. 7).

If we take the waypoints in the guidance sequence one at a time as individual goal points \mathbf{x}_{goal} , we can solve the given scenario as a series of motion planning problems (or “subplans”), calling FMT* from Section IV once for each instance, linking them together to form an overall solution to

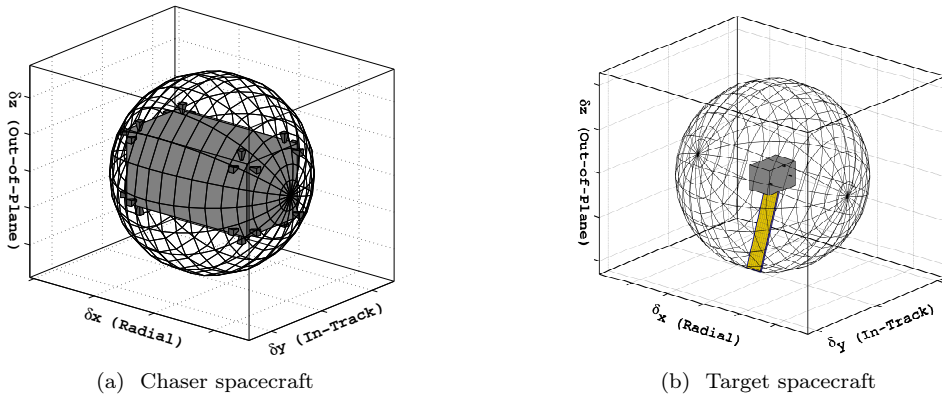


Fig. 9 Schematics of the chaser and target, together with their circumscribing spheres.

the problem. As our steering controller from Section IV A is attitude-independent, states $\mathbf{x} \in \mathbb{R}^d$ will be either $\mathbf{x}^T = [\delta x \ \delta y \ \delta \dot{x} \ \delta \dot{y}]$ with $d = 4$ (planar case) or $\mathbf{x}^T = [\delta x \ \delta y \ \delta z \ \delta \dot{x} \ \delta \dot{y} \ \delta \dot{z}]$ with $d = 6$ (non-planar case). We omit the attitude \mathbf{q} from the state during planning by assuming the existence of an attitude policy (as well as a stable attitude-trajectory-following controller) that produces $\mathbf{q}(t)$ from the state trajectory $\mathbf{x}(t)$; for illustration purposes, a simple nadir-pointing attitude profile is chosen to represent a mission that requires constant communication with the ground throughout the maneuver (note this is not enforced along actively-safe escape trajectories, which for each failure mode execute a simple “turn-burn-turn” policy that orients the closest available thruster as quickly as possible in the direction required to implement the necessary circularization burn). Given the hyper-rectangular shape of the state-space, we call upon the deterministic, low-dispersion d -dimensional Halton sequence [39] to sample positions and velocities. To improve sample densities, each subplan uses its own sample space defined around only its respective initial and goal waypoints, with some arbitrary threshold space added around them. Additionally, extra samples n_{goal} are taken inside each waypoint ball to facilitate convergence. For this multi-plan problem, we define the solution cost as the sum of individual subplan costs (if using trajectory smoothing, the endpoints between two plans will be merged identically to two edges within a plan, as described in Section V).

Before we proceed to the results, we make note of a few implementation details. First, for clarity we list the simulation parameters used in Table 1. Second, all position-related constraint-checking regard the chaser spacecraft as a point at its center of mass, with all other obstacles artificially inflated by the radius of its circumscribing sphere. Third and finally, all trajectory collision-checking

Table 1 List of parameters used during numerical experiments.

Chaser plume half-angle, β_{plume}	10°
Chaser plume height, H_{plume}	16 m
Chaser thruster fault tolerance, F	2
Cost threshold, \bar{J}	0.1–0.4 m/s
Dimension, d	4
Goal sample count, n_{goal}	0.04 n
Goal position tolerance, ϵ_r	3–8 m
Goal velocity tolerance, ϵ_v	0.1–0.5 m/s
Max. allocated thruster Δv magnitude, $\Delta v_{\text{max},k}$	∞ m/s
Max. commanded Δv -vector magnitude $\ \Delta \mathbf{v}_i\ $, Δv_{max}	∞ m/s
Max. plan duration, $T_{\text{plan,max}}$	∞ s
Min. plan duration, $T_{\text{plan,min}}$	0 s
Max. steering maneuver duration, T_{max}	$0.1 \cdot (2\pi/n_{\text{ref}})$
Min. steering maneuver duration, T_{min}	0 s
Sample count, n	50–400 per plan
Simulation timestep, Δt	$0.0005 \cdot (2\pi/n_{\text{ref}})$
Target antenna lobe height	75 m
Target antenna beamwidth	60°
Target KOZ semi-axes, $[\rho_{\delta x}, \rho_{\delta y}, \rho_{\delta z}]$	[35 50 15] m

is implemented by point-wise evaluation with a fixed time-step resolution Δt , using the analytic state transition equations Eq. (5) together with steering solutions from Section IV A to propagate graph edges; for speed, the line segments between points are excluded. Except near very sharp obstacle corners, this approximation is generally not a problem in practice (obstacles can always be inflated further to account for this). To improve performance, each obstacle primitive (ellipsoid, right-circular cone, hypercube, *etc.*) employs hierarchical collision-checking using hyper-spherical and/or hyper-rectangular bounding volumes to quickly prune points from consideration.

A Planar Motion Planning Solution

A representative solution to the posed planning scenario, both with and without the trajectory smoothing algorithm (Algorithm 2), is shown in Fig. 10. As shown, the planner successfully finds safe trajectories within each subplan, which are afterwards linked to form an overall solution. The state space of the first subplan shown at the bottom is essentially obstacle-free, as the chaser at this point is too far away from the target for plume impingement to come into play. This means every edge connection attempted here is added; so the first subplan illustrates well a discrete subset of the reachable states around \mathbf{x}_{init} and the unrestrained growth of FMT*. As the second subplan is reached, the effects of the Keep-Out-Zone position constraints come in to play, and we see edges

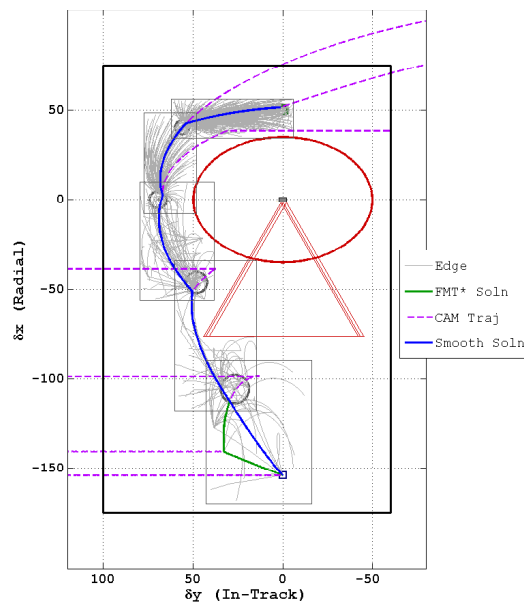


Fig. 10 Representative planar motion planning solution using the FMT* algorithm (Algorithm 1) with $n = 2000$ (400 per subplan), $\bar{J} = 0.3$ m/s, and relaxed waypoint convergence.

begin to take more leftward loops. In subplans 3 and 4, plume impingement begins to play a role. Finally, in subplan 5 at the top, where it becomes very cheap to move between states (as the spacecraft can simply coast to the right for free), we see the initial state connecting to nearly every sample in the subspace, resulting in a straight shot to the final goal. As is evident, straight-line path planning would not approximate these trajectories well, particularly near coasting arcs which our dynamics allow the spacecraft to transfer to for free.

To understand the smoothing process, examine Fig. 11. Here we see how the discrete trajectory sequence from our sampling-based algorithm may be smoothly and continuously deformed towards the unconstrained minimal-propellant trajectory (as outlined in Section V) until it meets trajectory constraints; if these constraints happen to be inactive, then the exact minimal-propellant trajectory is returned, as Fig. 11a shows. This computational approach is generally quite fast, assuming a well-implemented convex solver is used, as will be seen in the results of the next subsection.

The 2-norm Δv costs of the two reported trajectories in this example come to 0.835 m/s (unsmoothed) and 0.811 m/s (smoothed). Compare this to 0.641 m/s, the cost of the unconstrained direct solution that intercepts each of the goal waypoints on its way to rendezvousing with \mathbf{x}_{goal} (this trajectory exits the state-space along the positive in-track direction, a violation of our pro-

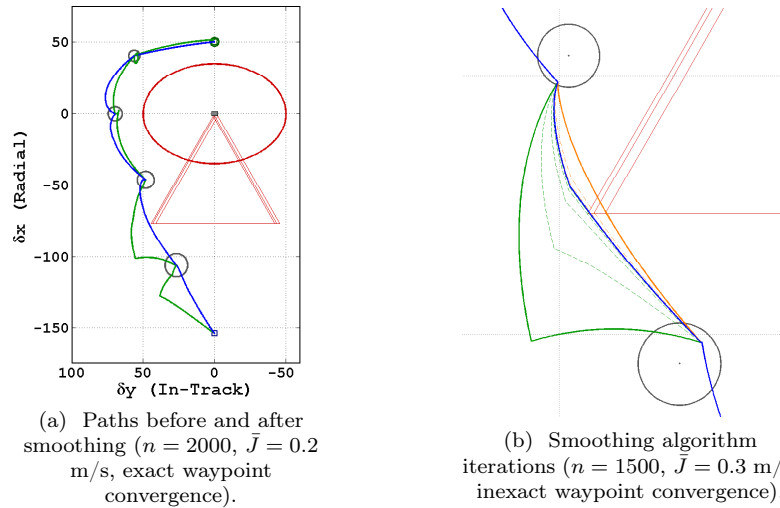


Fig. 11 Visualizing trajectory smoothing (Algorithm 2) for the solution shown in Fig. 10.

posed mission; hence its cost represents an under-approximation to the true optimal cost J^* of the constrained problem). This suggests that our solutions are quite close to the constrained optimum, and certainly on the right order of magnitude. Particularly with the addition of smoothing at lower sample counts, the approach appears to be a viable one for spacecraft planning.

If we compare the 2-norm Δv costs to the actual measured propellant consumption given by the sum total of all allocated thruster Δv magnitudes, which equal 1.06 m/s (unsmoothed) and 1.01 m/s (smoothed) respectively, we find increases of 27.0% and 24.5%; as expected, our 2-norm cost metric under-approximates the true propellant cost. For point-masses with isotropic control authority (*e.g.*, a steerable or gimballed thruster that is able to point freely in any direction), our cost metric would be exact. However, for our distributed attitude-dependent propulsion system (see Fig. 9a), it is clearly a reasonable proxy for allocated propellant use, returning values on the same order of magnitude. Though we cannot make a strong statement about our proximity to the propellant-optimal solution without directly optimizing over thruster Δv allocations, our solution clearly seems to promote low propellant consumption.

B Non-Planar Motion Planning Solution

For the non-planar case, representative smoothed and unsmoothed FMT* solutions can be found in Fig. 12. Here the spacecraft is required to move out-of-plane to survey the target from above before reaching the final goal position located radially above the target. The first subplan involves

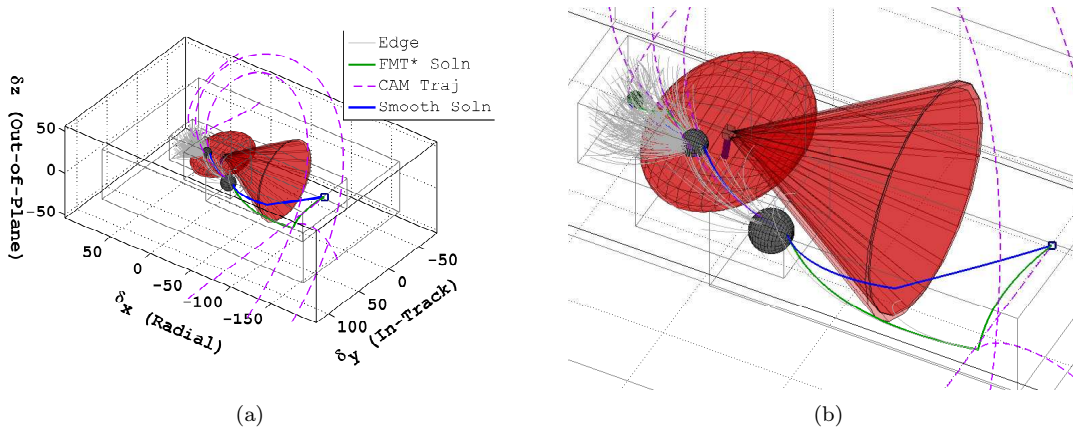


Fig. 12 Representative non-planar motion planning solution using the FMT* algorithm (Algorithm 1) with $n = 900$ (300 per subplan), $\bar{J} = 0.4$ m/s, and relaxed waypoint convergence.

a long reroute around the conical region spanned by the target spacecraft’s communication lobes. Because the chaser begins in a coplanar circular orbit at \mathbf{x}_{init} , most steering trajectories require a fairly large cost to maneuver out-of-plane to the first waypoint. Consequently, relatively few edges are added that both lie in the reachable set of \mathbf{x}_{init} and safely avoid the large conical obstacles. As we progress to the second and third subplans, the corresponding trees become denser (more steering trajectories are both safe and within our cost threshold \bar{J}) as the state space becomes freer. Compared with the planar case, the extra degree-of-freedom associated with the out-of-plane dimension appears to allow more edges ahead of the target in the in-track direction than before, likely because now the exhaust plumes generated by the chaser are well out-of-plane from the target spacecraft. Hence the spacecraft smoothly and tightly curls around the ellipsoidal KOZ to the goal.

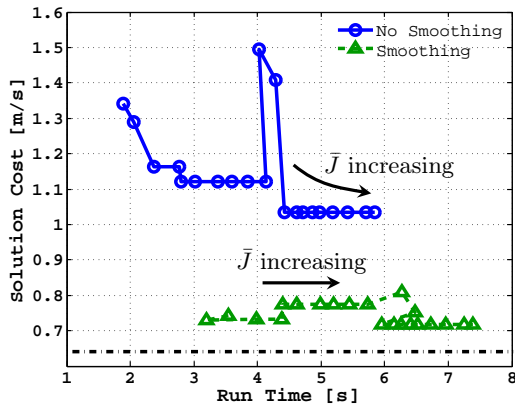
The 2-norm Δv costs for this example come to 0.611 m/s (unsmoothed) and 0.422 m/s (smoothed). Counter-intuitively, these costs are on the same order of magnitude and slightly cheaper than the planar case; the added freedom given by the out-of-plane dimension appears to outweigh the high costs typically associated with inclination changes and out-of-plane motion. The 2-norm cost values correspond to total thruster Δv allocation costs of 0.893 m/s and 0.620 m/s, respectively – increases of 46% and 47% above their counterpart cost metric values. Again, our cost metric appears to be a reasonable proxy for actual propellant use.

C Performance Evaluation

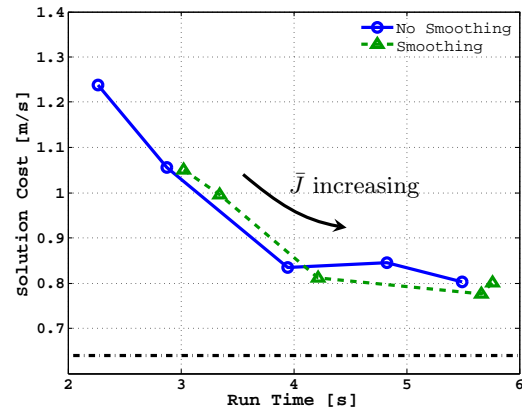
To evaluate the performance of our approach, an assessment is necessary of solution quality as a function of planning parameters, most importantly the number of samples n taken and the reachability set cost threshold \bar{J} . As proven in Section IV D, the solution cost will eventually reduce to the optimal value as we increase the sample size n . Additionally, one can increase the cost threshold \bar{J} used for nearest-neighbor identification so that more connections are explored. However, both come at the expense of running time. To understand the effects of these changes on quality, particularly at finite sample counts where the asymptotic guarantees of FMT* do not necessarily imply cost improvements, we measure the cost versus computation time for the planar planning scenario parameterized over several values of each n and \bar{J} .

Results are reported in Figs. 13–14. For a given sequence of sample count/cost threshold pairs, we ran our algorithm in each configuration and recorded the total cost of *successful* runs and their respective run times [45] as measured by wall clock time. Note that all samples were drawn and their interconnecting steering problems were solved *offline* per our discussion in Section IV C. Only the *online* components of each call constitute the run times reported, including running FMT* with collision-checking and graph construction, as these are the only elements critical to the real-time implementability of the approach; everything else may be computed offline on ground computers where computation is less restricted, and later uplinked to the spacecraft or stored onboard prior to mission launch. See Section IV C for details. Samples were stored as a $d \times n$ array, while inter-sample steering controls $\Delta \mathbf{v}_i^*$ and times τ_i were precomputed as $n \times n$ arrays of $d/2 \times N$ and $N \times 1$ array elements, respectively. To reduce memory requirements, steering trajectories \mathbf{x}^* and \mathbf{q} were generated online through Eq. (5) and our nadir-pointing assumption, though in principle they could have easily been stored as well to save additional computation time.

Figure 13 reports the effects on the solution cost of varying the nearest-neighbor search threshold \bar{J} while keeping n fixed. As described in Section IV B, \bar{J} determines the size of state reachability sets and hence the number of candidate neighbors evaluated during graph construction. Generally, this means an improvement in cost at the expense of extra processing; though there are exceptions as in Fig. 13a at $\bar{J} \approx 0.3$ m/s. Likely this arises from a neighbor that is found and connected to



(a) Exact waypoint convergence ($n = 2000$).



(b) Inexact waypoint convergence ($n = 2000$).

Fig. 13 Algorithm performance for the given LEO proximity operations scenario as a function of varying cost threshold ($\bar{J} \in [0.2, 0.4]$) with n held constant.

(at the expense of another, since FMT* only adds one edge per nearest-neighborhood) which leads to a particular graph change for which *exact* termination at the goal waypoint is more expensive than usual. Indeed we see that *for the same sample distribution* this does not occur, as shown in the other case where inexact convergence is permitted.

We can also vary the sample count n while holding \bar{J} constant. From Figs. 13a–13b, we select $\bar{J} = 0.22$ m/s and 0.3 m/s, respectively, for each of the two cases (the values which suggest the best solution cost per unit of run time). Repeating the simulation for varying sample count values, we obtain Fig. 14. Note the general downward trend as run time increases (corresponding to larger sample counts), indicating the classic trade-off in sampling-based planning. However, there is bumpiness. Similar to before, this is likely due to new connections previously unavailable at lower sample counts which cause a slightly different graph with an unlucky jump in propellant cost. This reinforces the well-known need to tune n and \bar{J} before applying sampling-based planners.

As the figures show, the utility of trajectory smoothing is clearly affected by the fidelity of the planning simulation. In each, trajectory smoothing yields a much larger improvement in cost at modest increases in computation time when we require exact waypoint convergence. It provides little improvement, on the other hand, when we relax these waypoint tolerances; FMT* (with goal region sampling) seems to return trajectories with costs much closer to the optimum in such cases, making the additional overhead of smoothing less favorable. This conclusion is likely highly problem-dependent; these tools must always be tested and tuned to the particular application.

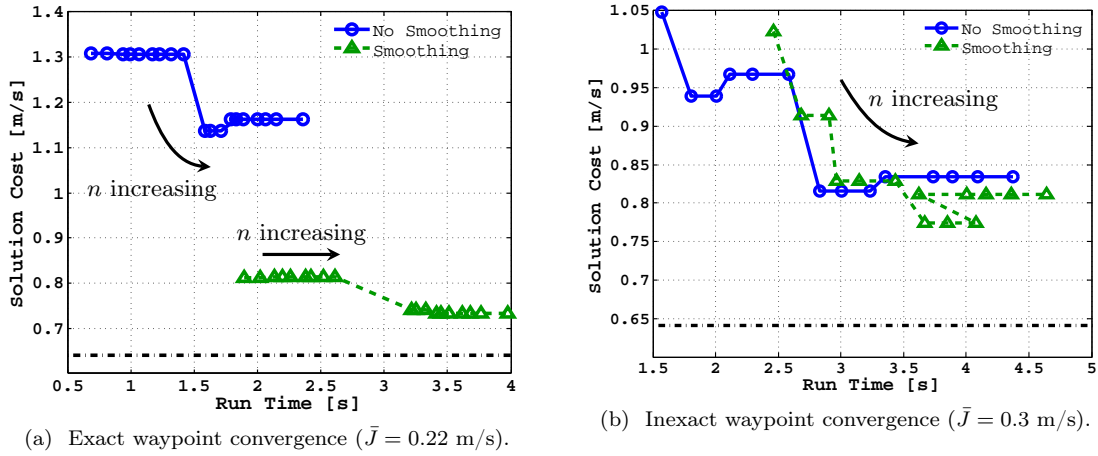


Fig. 14 Algorithm performance for the given LEO proximity operations scenario as a function of varying sample count ($n \in [650, 2000]$) with \bar{J} held constant.

Note that the overall run times for each simulation are on the order of 1-5 seconds, including smoothing. This clearly indicates that FMT* can return high quality solutions in real-time for spacecraft proximity operations. Though run on a computer currently unavailable to spacecraft, we hope that our examples serve as a reasonable proof-of-concept; we expect that with a more efficient coding language and implementation, our approach would be competitive on spacecraft hardware.

VII Conclusions

A technique has been presented for efficiently automating minimum-propellant guidance during near-circular orbit proximity operations, enabling the computation of near-optimal collision-free trajectories in real time (on the order of 1-5 seconds for our numerical examples). The approach allows our modified version of the FMT* sampling-based motion planning algorithm to approximate the solution to the minimal-propellant trajectory control problem Eq. (1) under impulsive Clohessy-Wiltshire-Hill (CWH) dynamics. The method begins by discretizing the feasible space of Eq. (1) through state space sampling in the CWH Local-Vertical Local-Horizontal (LVLH) frame. Next, state samples and their forward *reachability sets*, which we have shown comprise sets bounded by unions of ellipsoids taken over steering maneuver duration, are precomputed offline and stored onboard the spacecraft together with all pairwise steering solutions. Finally, the FMT* algorithm (with built-in trajectory smoothing) is called online to efficiently construct a tree of trajectories through the feasible state space towards a goal region, returning a solution that satisfies a broad

range of trajectory constraints (*e.g.*, plume impingement, control allocation feasibility, obstacle avoidance, *etc.*) or else reporting failure. If desired, additional post-processing using the techniques outlined in Section V can be employed to reduce solution propellant cost.

The key breakthrough of our solution for autonomous spacecraft guidance is its judicious distribution of computations; in essence, only what *must* be computed onboard, such as collision-checking and graph construction, is computed online – everything else, including the most intensive computations, are relegated to the ground where computational effort and run time are less critical. Furthermore, only minimal information (steering problem control trajectories, costs, and nearest-neighbor sets) requires storage on the spacecraft. Though we have illustrated through simulations the ability to tackle a particular minimum-propellant LEO homing maneuver problem, it should be noted that the methodology applies equally well to other objectives, such as the minimum-time problem, and can be generalized to other dynamic models and environments. The approach is flexible enough to handle non-convexity and mixed state-control-time constraints without compromising real-time implementability, so long as constraint function evaluation is relatively efficient. In short, the proposed approach appears to be useful for automating the mission planning process for spacecraft proximity operations, enabling real-time computation of low cost trajectories.

In future work, the authors plan to demonstrate the proposed approach in a number of other proximity operations scenarios, including optimal deep-space guidance, pinpoint asteroid descent, and onboard a set of free-flying, air-bearing robots. However, the proposed planning framework for impulsively-actuated spacecraft offers several other interesting avenues for future research. For example, though nothing in the methodology forbids it outside of computational limitations, it would be interesting to revisit the problem with attitude states included in the planning process (instead of abstracted away, as we have done here by assuming an attitude profile). This would allow direct inclusion of attitude constraints into maneuver planning (*e.g.*, enforcing line-of-sight, keeping solar panels oriented towards the Sun to stay power positive, maintaining a communication link between the chaser antenna and ground, *etc.*). Also of interest would be other actively-safe policies that relax the need to circularize escape orbits (potentially costly in terms of propellant use) or which mesh better with trajectory smoothing, without the need to add compensating impulses (see Section V).

Extensions to dynamic obstacles (such as debris or maneuvering spacecraft, which are unfixed in the LVLH frame), elliptical target orbits, higher-order gravitation, curvilinear coordinates, or dynamics under relative orbital elements also represent key research topics vital to extending the method's applicability to more general maneuvers. Finally, memory and run time performance evaluations of our algorithms on space-like hardware would be necessary in assessing their true benefit to spacecraft planning in practice.

Appendix A: Optimal Circularization Under Impulsive CWH Dynamics

As detailed in Section III C 1, a vital component of our CAM policy is the generation of one-burn minimal-propellant transfers to circular orbits above or below the target spacecraft orbit. Assuming a failure occurs at state $\mathbf{x}(t_{\text{fail}}) = \mathbf{x}_{\text{fail}}$, the problem we wish to solve to satisfy Definition 4 is:

$$\begin{aligned}
\text{Given:} \quad & \text{Failure state } \mathbf{x}_{\text{fail}}, \text{ and CAM } \mathbf{u}_{\text{CAM}}(t_{\text{fail}} \leq t < T_h^-) \triangleq \mathbf{0}, \mathbf{u}_{\text{CAM}}(T_h) \triangleq \Delta \mathbf{v}_{\text{circ}}(\mathbf{x}(T_h)) \\
\text{minimize} \quad & \Delta v_{\text{circ}}^2(T_h) \\
\text{subject to} \quad & \mathbf{x}_{\text{CAM}}(t_{\text{fail}}) = \mathbf{x}_{\text{fail}} \quad \text{Initial Condition} \\
& \mathbf{x}_{\text{CAM}}(T_h^+) \in \mathcal{X}_{\text{invariant}} \quad \text{Invariant Set Termination} \\
& \dot{\mathbf{x}}_{\text{CAM}}(t) = f(\mathbf{x}_{\text{CAM}}(t), \mathbf{0}, t), \text{ for all } t_{\text{fail}} \leq t \leq T_h \quad \text{System Dynamics} \\
& \mathbf{x}_{\text{CAM}}(t) \notin \mathcal{X}_{\text{KOZ}}, \text{ for all } t_{\text{fail}} \leq t \leq T_h \quad \text{KOZ Collision Avoidance}
\end{aligned}$$

Due to the analytical descriptions of state transitions as given by Eq. (5), it is a straightforward task to express the decision variable T_h , invariant set constraint, and objective function analytically in terms of $\theta(t) = n_{\text{ref}}(t - t_0)$, the polar angle of the target spacecraft. The problem is therefore one-dimensional in terms of θ . We can reduce the invariant set termination constraint to an invariant set positioning constraint if we ensure the spacecraft ends up at a position inside $\mathcal{X}_{\text{invariant}}$ and circularize the orbit, since $\mathbf{x}(\theta_{\text{circ}}^+) = \mathbf{x}(\theta_{\text{circ}}^-) + [\Delta \mathbf{v}_{\text{circ}}(\theta_{\text{circ}})] \in \mathcal{X}_{\text{invariant}}$. Denote $\theta_{\text{circ}} = n_{\text{ref}}(T_h - t_0)$ as the target anomaly at which we enforce circularization. Now, suppose the failure state $\mathbf{x}(t)$ satisfies the collision avoidance constraint with the KOZ (otherwise the CAM is infeasible and we conclude \mathbf{x} is unsafe). We can set $\theta_{\text{min}} = n_{\text{ref}}(t - t_0)$ and integrate the coasting dynamics forward until the chaser touches the boundary of the KOZ ($\theta_{\text{max}} = \theta_{\text{collision}}^-$) or until we have reached one full orbit

($\theta_{\max} = \theta_{\min} + 2\pi$) such that, between these two bounds, the CAM trajectory satisfies the dynamics and contains only the coasting segment outside of the KOZ. Replacing the dynamics and collision avoidance constraints with the bounds on θ as a box constraint, the problem now reduces to:

$$\begin{aligned} & \underset{\theta_{\text{circ}}}{\text{minimize}} && \Delta v_{\text{circ}}^2(\theta_{\text{circ}}) \\ & \text{subject to} && \theta_{\min} \leq \theta_{\text{circ}} \leq \theta_{\max} && \text{Theta Bounds} \\ & && \delta x^2(\theta_{\text{circ}}^-) \geq \rho_{\delta x}^2 && \text{Invariant Set Positioning} \end{aligned}$$

Restricting our search range to $\theta \in [\theta_{\min}, \theta_{\max}]$, this is a function of one variable and one constraint, something we can easily optimize analytically using the method of Lagrange multipliers. To solve, we seek to minimize the Lagrangian, $\mathcal{L} = \Delta v_{\text{circ}}^2 + \lambda g_{\text{circ}}$, where $g_{\text{circ}}(\theta) = \rho_{\delta x}^2 - \delta x^2(\theta_{\text{circ}}^-)$. There are two cases to consider:

a Case 1: Inactive Invariant Set Positioning Constraint We set $\lambda = 0$ such that $\mathcal{L} = \Delta v_{\text{circ}}^2$.

Candidate optimizers θ^* must satisfy $\nabla_{\theta} \mathcal{L}(\theta^*) = 0$. Taking the gradient of \mathcal{L} ,

$$\begin{aligned} \nabla_{\theta} \mathcal{L} &= \frac{\partial \Delta v_{\text{circ}}^2}{\partial \theta} = \left[\frac{3}{4} (3n_{\text{ref}} \delta x_{\text{fail}} + 2\delta \dot{y}_{\text{fail}})^2 - \frac{3}{4} \delta \dot{x}_{\text{fail}}^2 + n_{\text{ref}}^2 \delta z_{\text{fail}}^2 - \delta \dot{z}_{\text{fail}}^2 \right] \sin 2\theta \\ &+ \left[\frac{3}{2} \delta \dot{x}_{\text{fail}} (3n_{\text{ref}} \delta x_{\text{fail}} + 2\delta \dot{y}_{\text{fail}}) - 2n_{\text{ref}} \delta \dot{z}_{\text{fail}} \delta z_{\text{fail}} \right] \cos 2\theta \end{aligned}$$

and setting $\nabla_{\theta} \mathcal{L}(\theta^*) = 0$, we find that:

$$\tan 2\theta^* = \frac{-\left(\frac{3}{2} \delta \dot{x}_{\text{fail}} (3n_{\text{ref}} \delta x_{\text{fail}} + 2\delta \dot{y}_{\text{fail}}) - 2n_{\text{ref}} \delta \dot{z}_{\text{fail}} \delta z_{\text{fail}}\right)}{\frac{3}{4} (3n_{\text{ref}} \delta x_{\text{fail}} + 2\delta \dot{y}_{\text{fail}})^2 - \frac{3}{4} \delta \dot{x}_{\text{fail}}^2 + n_{\text{ref}}^2 \delta z_{\text{fail}}^2 - \delta \dot{z}_{\text{fail}}^2}$$

Denote the set of candidate solutions that satisfy Case 1 by Θ_1^* .

b Case 2: Active Invariant Set Positioning Constraint Here the chaser attempts to circularize its orbit at the boundary of the zero-thrust RIC shown in Fig. 4a. The positioning constraint is active, and therefore $g_{\text{circ}}(\theta) = \rho_{\delta x}^2 - \delta x^2(\theta_{\text{circ}}^-) = 0$. This is equivalent to finding where the coasting trajectory from $\mathbf{x}(t)$ crosses $\delta x(\theta) = \pm \rho_{\delta x}$ for $\theta \in [\theta_{\min}, \theta_{\max}]$. This can be achieved using standard root-finding algorithms. Denote the set of candidate solutions that satisfy Case 2 by Θ_2^* .

c Solution to the Minimal-Cost Circularization Burn The global optimizer θ^* either lies on the boundary of the box constraint, at an unconstrained optimum ($\theta \in \Theta_1^*$), or at the boundary of the zero-thrust RIC ($\theta \in \Theta_2^*$), all of which are economically obtained through either numerical integration or root-finding solver. Therefore, the minimal-cost circularization burn time T_h^* satisfies:

$$\theta^* = n_{\text{ref}}(T_h^* - t_0) = \arg \min_{\theta \in \{\theta_{\min}, \theta_{\max}\} \cup \Theta_1^* \cup \Theta_2^*} \Delta v_{\text{circ}}^2(\theta)$$

If no solution exists (which can happen if and only if \mathbf{x}_{fail} starts inside the KOZ), the circularization CAM is declared unsafe. Otherwise, the CAM is saved for future trajectory feasibility verification.

Appendix B: Intermediate Results for the FMT* Optimality Proof

We report here a number of useful lemmas concerning bounds on the trajectory costs between samples which are used throughout the asymptotic optimality proof for FMT* in Section IV. We begin with the proof of Lemma 7, which relates the propellant-burn cost function Eq. (15) between points \mathbf{x}_0 and \mathbf{x}_f to the norm of the stacked Δv -vector $\|\Delta \mathbf{V}\| = \|\mathbf{x}_f - \Phi(t_f, t_0)\mathbf{x}_0\|_{\mathbf{G}^{-1}}$. We then provide a lemma bounding the sizes of the minimum and maximum eigenvalues of \mathbf{G} , useful for bounding reachable volumes from \mathbf{x}_0 . Finally, we prove Lemma 9 which forms the basis of our asymptotic optimality analysis for FMT*. Here $\Phi(t_f, t_0) = e^{\mathbf{A}T}$ is the state transition matrix, $T = t_f - t_0$ is the maneuver duration, and \mathbf{G} is the $N = 2$ impulse Gramian matrix:

$$\mathbf{G}(T) = \Phi_v \Phi_v^{-1} = \begin{bmatrix} e^{\mathbf{A}T} \mathbf{B} & \mathbf{B} \end{bmatrix} \begin{bmatrix} e^{\mathbf{A}T} \mathbf{B} & \mathbf{B} \end{bmatrix}^T, \quad (\text{B1})$$

where $\Phi_v(t, \{\tau_i\}_i)$ is the aggregate Δv transition matrix corresponding to burn times $\{\tau_i\}_i = \{t_0, t_f\}$.

Lemma 7 (Fuel Burn Cost Bounds). *For the cost function in Eq. (15), we have the following upper and lower bounds:*

$$\|\Delta \mathbf{V}\| \leq J(\mathbf{x}_0, \mathbf{x}_f) \leq \sqrt{2} \|\Delta \mathbf{V}\|.$$

Proof. For the upper bound, note that by the Cauchy-Schwarz inequality we have $J = \|\Delta \mathbf{v}_1\| \cdot 1 + \|\Delta \mathbf{v}_2\| \cdot 1 \leq \sqrt{\|\Delta \mathbf{v}_1\|^2 + \|\Delta \mathbf{v}_2\|^2} \cdot \sqrt{1^2 + 1^2}$. That is, $J \leq \sqrt{2}\|\Delta \mathbf{V}\|$. Similarly, for the lower bound, note that: $J = \sqrt{(\|\Delta \mathbf{v}_1\| + \|\Delta \mathbf{v}_2\|)^2} \geq \sqrt{\|\Delta \mathbf{v}_1\|^2 + \|\Delta \mathbf{v}_2\|^2} = \|\Delta \mathbf{V}\|$. \square

Lemma 15 (Bounds on Gramian Eigenvalues). *Let T_{\max} be less than one orbital period for the system dynamics of Section II C, and let $\mathbf{G}(T)$ be defined as in Eq. (B1). Then there exist constants $M_{\min}, M_{\max} > 0$ such that $\lambda_{\min}(\mathbf{G}(T)) \geq M_{\min}T^2$ and $\lambda_{\max}(\mathbf{G}(T)) \leq M_{\max}$ for all $T \in (0, T_{\max}]$.*

Proof. We bound the maximum eigenvalue of \mathbf{G} through norm considerations, yielding $\lambda_{\max}(\mathbf{G}(T)) \leq (\|e^{\mathbf{A}T}\mathbf{B}\| + \|\mathbf{B}\|)^2 \leq (e^{\|\mathbf{A}\|T_{\max}} + 1)^2$, and take $M_{\max} = (e^{\|\mathbf{A}\|T_{\max}} + 1)^2$. As long as T_{\max} is less than one orbital period, $\mathbf{G}(T)$ only approaches singularity near $T = 0$ [36]. Explicitly Taylor-expanding $\mathbf{G}(T)$ about $T = 0$ reveals that $\lambda_{\min}(\mathbf{G}(T)) = T^2/2 + O(T^3)$ for small T , and thus $\lambda_{\min}(\mathbf{G}(T)) = \Omega(T^2)$ for all $T \in (0, T_{\max}]$. \square

Lemma 9 (Steering with Perturbed Endpoints). *For a given steering trajectory $\mathbf{x}(t)$ with initial time t_0 and final time t_f , let $\mathbf{x}_0 := \mathbf{x}(t_0)$, $\mathbf{x}_f := \mathbf{x}(t_f)$, $T := t_f - t_0$, and $J := J(\mathbf{x}_0, \mathbf{x}_f)$. Consider now the steering trajectory $\tilde{\mathbf{x}}(t)$ between perturbed start and end points $\tilde{\mathbf{x}}_0 = \mathbf{x}_0 + \delta \mathbf{x}_0$ and $\tilde{\mathbf{x}}_f = \mathbf{x}_f + \delta \mathbf{x}_f$.*

Case 1: $T = 0$. *There exists a perturbation center $\delta \mathbf{x}_c$ (consisting of only a position shift) with $\|\delta \mathbf{x}_c\| = O(J^2)$ such that if $\|\delta \mathbf{x}_0\| \leq \eta J^3$ and $\|\delta \mathbf{x}_f - \delta \mathbf{x}_c\| \leq \eta J^3$ then $J(\tilde{\mathbf{x}}_0, \tilde{\mathbf{x}}_f) \leq J(1 + 4\eta + O(J))$ and the spatial deviation of the perturbed trajectory from $\mathbf{x}(t)$ is $O(J)$.*

Case 2: $T > 0$. *If $\|\delta \mathbf{x}_0\| \leq \eta J^3$ and $\|\delta \mathbf{x}_f\| \leq \eta J^3$ then $J(\tilde{\mathbf{x}}_0, \tilde{\mathbf{x}}_f) \leq J(1 + O(\eta J^2 T^{-1}))$ and the spatial deviation of the perturbed trajectory from $\mathbf{x}(t)$ is $O(J)$.*

Proof. For bounding the perturbed cost, we consider the two cases separately.

Case 1: $T = 0$. Then 2-impulse steering degenerates to a single impulse $\Delta \mathbf{v}$; that is, $\mathbf{x}_f = \mathbf{x}_0 + \mathbf{B}\Delta \mathbf{v}$ with $\|\Delta \mathbf{v}\| = J$. To aid in the ensuing analysis, we write the position and velocity components of each state $\mathbf{x} = [\mathbf{r}^T \ \mathbf{v}^T]^T$ as $\mathbf{r} = [\mathbf{I} \ \mathbf{0}]\mathbf{x}$ and $\mathbf{v} = [\mathbf{0} \ \mathbf{I}]\mathbf{x}$. Note that since $T = 0$, we have $\mathbf{r}_f = \mathbf{r}_0$ and $\mathbf{v}_f = \mathbf{v}_0 + \Delta \mathbf{v}$. We pick the perturbed steering duration $\tilde{T} = J^2$ (which will provide an upper bound on the optimal steering cost) and expand the steering system (Eq. (5)) for small time \tilde{T} as

$$\mathbf{r}_f + \delta \mathbf{r}_f = \mathbf{r}_0 + \delta \mathbf{r}_0 + \tilde{T}(\mathbf{v}_0 + \delta \mathbf{v}_0 + \widetilde{\Delta \mathbf{v}_1}) + O(\tilde{T}^2) \quad (\text{B2})$$

$$\mathbf{v}_f + \delta \mathbf{v}_f = \mathbf{v}_0 + \delta \mathbf{v}_0 + \widetilde{\Delta \mathbf{v}}_1 + \widetilde{\Delta \mathbf{v}}_2 + \tilde{T} \left(\mathbf{A}_{21}(\mathbf{r}_0 + \delta \mathbf{r}_0) + \mathbf{A}_{22}(\mathbf{v}_0 + \delta \mathbf{v}_0 + \widetilde{\Delta \mathbf{v}}_1) \right) + O(\tilde{T}^2) \quad (\text{B3})$$

where $\mathbf{A}_{21} = \begin{bmatrix} 3n_{\text{ref}}^2 & 0 & 0 \\ 0 & 0 & 0 \\ 0 & 0 & -n_{\text{ref}}^2 \end{bmatrix}$ and $\mathbf{A}_{22} = \begin{bmatrix} 0 & 2n_{\text{ref}} & 0 \\ -2n_{\text{ref}} & 0 & 0 \\ 0 & 0 & 0 \end{bmatrix}$. Solving Eq. (B2) for $\widetilde{\Delta \mathbf{v}}_1$ to first order, we find $\widetilde{\Delta \mathbf{v}}_1 = \tilde{T}^{-1}(\delta \mathbf{r}_f - \delta \mathbf{r}_0) - \mathbf{v}_0 - \delta \mathbf{v}_0 + O(\tilde{T})$. By selecting $\delta \mathbf{x}_c = [\tilde{T} \mathbf{v}_0^T \mathbf{0}^T]^T$ (note: $\|\delta \mathbf{x}_c\| = J^2 \|\mathbf{v}_0\| = O(J^2)$) and supposing that $\|\delta \mathbf{x}_0\| \leq \eta J^3$ and $\|\delta \mathbf{x}_f - \delta \mathbf{x}_c\| \leq \eta J^3$, we have that:

$$\|\widetilde{\Delta \mathbf{v}}_1\| \leq J^{-2}(\|\delta \mathbf{x}_0\| + \|\delta \mathbf{x}_f - \delta \mathbf{x}_c\|) + \|\delta \mathbf{x}_0\| + O(J^2) = 2\eta J + O(J^2).$$

Now solving Eq. (B3) for $\widetilde{\Delta \mathbf{v}}_2 = \Delta \mathbf{v} + (\delta \mathbf{v}_f - \delta \mathbf{v}_0) - \widetilde{\Delta \mathbf{v}}_1 + O(J^2)$, and taking norm of both sides:

$$\|\widetilde{\Delta \mathbf{v}}_2\| \leq \|\Delta \mathbf{v}\| + (\|\delta \mathbf{x}_0\| + \|\delta \mathbf{x}_f - \delta \mathbf{x}_c\|) + 2\eta J + O(J^2) \leq J + 2\eta J + O(J^2).$$

Therefore the perturbed cost satisfies:

$$J(\tilde{\mathbf{x}}_0, \tilde{\mathbf{x}}_f) \leq \|\widetilde{\Delta \mathbf{v}}_1\| + \|\widetilde{\Delta \mathbf{v}}_2\| \leq J(1 + 4\eta + O(J)).$$

Case 2: $T > 0$. We pick $\tilde{T} = T$ to compute an upper bound on the perturbed cost. Applying the explicit form of the steering control (Eq. (14)) along with the norm bound $\|\Phi_v^{-1}\| = \lambda_{\min}(\mathbf{G})^{-1/2} \leq M_{\min}^{-1/2} T^{-1}$ from Lemma 15, we have:

$$\begin{aligned} J(\tilde{\mathbf{x}}_0, \tilde{\mathbf{x}}_f) &\leq \|\Phi_v^{-1}(t_f, \{t_0, t_f\})(\tilde{\mathbf{x}}_f - \Phi(t_f, t_0)\tilde{\mathbf{x}}_0)\| \\ &\leq \|\Phi_v^{-1}(\mathbf{x}_f - \Phi \mathbf{x}_0)\| + \|\Phi_v^{-1} \delta \mathbf{x}_f\| + \|\Phi_v^{-1} \Phi \delta \mathbf{x}_0\| \\ &\leq J + M_{\min}^{-1/2} T^{-1} \|\delta \mathbf{x}_f\| + M_{\min}^{-1/2} T^{-1} e^{\|\mathbf{A}\| T_{\max}} \|\delta \mathbf{x}_0\| \leq J(1 + O(\eta J^2 T^{-1})). \end{aligned}$$

In both cases, the deviation of the perturbed steering trajectory (call it $\tilde{\mathbf{x}}(t)$) from its closest point on the original trajectory is bounded (quite conservatively) by the maximum propagation of the difference in initial conditions; that is, the initial disturbance $\delta \mathbf{x}_0$ plus the difference in intercept

burns $\widetilde{\Delta\mathbf{v}}_1 - \Delta\mathbf{v}_1$, over the maximum maneuver duration T_{\max} . Thus,

$$\|\tilde{\mathbf{x}}(t) - \mathbf{x}(t)\| \leq e^{\|\mathbf{A}\|T_{\max}} \left(\|\delta\mathbf{x}_0\| + \|\widetilde{\Delta\mathbf{v}}_1\| + \|\Delta\mathbf{v}_1\| \right) \leq e^{\|\mathbf{A}\|T_{\max}} (\eta J^3 + 2J + o(J)) = O(J)$$

where we have used $\|\Delta\mathbf{v}_1\| \leq J$ and $\|\widetilde{\Delta\mathbf{v}}_1\| \leq J(\tilde{\mathbf{x}}_0, \tilde{\mathbf{x}}_f) \leq J + o(J)$ from our above arguments. \square

Acknowledgments

This work was supported by an Early Career Faculty grant from NASA's Space Technology Research Grants Program (Grant NNX12AQ43G).

References

- [1] Dannemiller, D. P., "Multi-Maneuver Clohessy-Wiltshire Targeting," *AAS Astrodynamics Specialist Conference*, Girdwood, AK, July 2011, pp. 1–15.
- [2] Hablani, H. B., Tapper, M. L., and Dana Bashian, D. J., "Guidance and Relative Navigation for Autonomous Rendezvous in a Circular Orbit," *AIAA Journal of Guidance, Control, and Dynamics*, Vol. 25, No. 3, 2002, pp. 553–562.
- [3] Naasz, B. J., "Safety Ellipse Motion with Coarse Sun Angle Optimization," *Proc. of the NASA GSFC Flight Mechanics Symposium*, Greenbelt, MD, Oct. 2005, pp. 1–13.
- [4] Gaylor, D. E. and Barbee, B. W., "Algorithms for Safe Spacecraft Proximity Operations," *AAS Meeting*, Vol. 127 of *Advances in the Astronautical Sciences*, Seattle, WA, Jan. 2007, pp. 1–20.
- [5] Develle, M., Xu, Y., Pham, K., and Chen, G., "Fast Relative Guidance Approach for Autonomous Rendezvous and Docking Control," *Proc. of SPIE*, Vol. 8044 of *Sensors and Systems for Space Applications IV*, Orlando, FL, apr 2011, pp. 80440F.1–80440F.15.
- [6] Lopez, I. and McInnes, C. R., "Autonomous Rendezvous using Artificial Potential Function Guidance," *AIAA Journal of Guidance, Control, and Dynamics*, Vol. 18, No. 2, March 1995, pp. 237–241.
- [7] Muñoz, J. D. and Fitz Coy, N. G., "Rapid Path-Planning Options for Autonomous Proximity Operations of Spacecraft," *AAS Astrodynamics Specialist Conference*, Toronto, Canada, Aug. 2010, pp. 1–24.
- [8] Harris, M. W. and Açikmeşe, B., "Lossless Convexification of Non-Convex Optimal Control Problems for State Constrained Linear Systems," *Automatica*, Vol. 50, No. 9, 2014, pp. 2304–2311.
- [9] Breger, L. and How, J. P., "Safe Trajectories for Autonomous Rendezvous of Spacecraft," *AIAA Journal of Guidance, Control, and Dynamics*, Vol. 31, No. 5, 2008, pp. 1478–1489.

- [10] Vazquez, R., Gavilan, F., and Camacho, E. F., “Trajectory Planning for Spacecraft Rendezvous with On/Off Thrusters,” *IFAC World Congress*, Vol. 18, Milano, Italy, Aug. 2011, pp. 8473–8478.
- [11] Lu, P. and Liu, X., “Autonomous Trajectory Planning for Rendezvous and Proximity Operations by Conic Optimization,” *AIAA Journal of Guidance, Control, and Dynamics*, Vol. 36, No. 2, March 2013, pp. 375–389.
- [12] Liu, X. and Lu, P., “Solving Nonconvex Optimal Control Problems by Convex Optimization,” *AIAA Journal of Guidance, Control, and Dynamics*, Vol. 37, No. 3, May 2014, pp. 750–765.
- [13] Luo, Y.-Z., Liang, L.-B., Wang, H., and Tang, G.-J., “Quantitative Performance for Spacecraft Rendezvous Trajectory Safety,” *AIAA Journal of Guidance, Control, and Dynamics*, Vol. 34, No. 4, July 2011, pp. 1264–1269.
- [14] Richards, A., Schouwenaars, T., How, J. P., and Feron, E., “Spacecraft Trajectory Planning With Avoidance Constraints Using Mixed-Integer Linear Programming,” *AIAA Journal of Guidance, Control, and Dynamics*, Vol. 25, No. 4, 2002, pp. 755–765.
- [15] LaValle, S. M. and Kuffner, J. J., “Randomized Kinodynamic Planning,” *International Journal of Robotics Research*, Vol. 20, No. 5, 2001, pp. 378–400.
- [16] Frazzoli, E., “Quasi-Random Algorithms for Real-Time Spacecraft Motion Planning and Coordination,” *Acta Astronautica*, Vol. 53, No. 4–10, Aug. 2003, pp. 485–495.
- [17] Phillips, J. M., Kavradi, L. E., and Bedrossian, N., “Spacecraft Rendezvous and Docking with Real-Time, Randomized Optimization,” *AIAA Conf. on Guidance, Navigation and Control*, Austin, TX, Aug. 2003, pp. 1–11.
- [18] Kobilarov, M. and Pellegrino, S., “Trajectory Planning for CubeSat Short-Time-Scale Proximity Operations,” *AIAA Journal of Guidance, Control, and Dynamics*, Vol. 37, No. 2, March 2014, pp. 566–579.
- [19] Haight, M. and Duncan, G., “Modeling Common Cause Failures of Thrusters on ISS Visiting Vehicles,” Tech. rep., NASA, Jan. 2014, Available at <http://ntrs.nasa.gov/search.jsp?R=20140004797>.
- [20] Weiss, A., Baldwin, M., Petersen, C., Erwin, R. S., and Kolmanovsky, I. V., “Spacecraft Constrained Maneuver Planning for Moving Debris Avoidance Using Positively Invariant Constraint Admissible Sets,” *American Control Conference*, Washington, DC, June 2013, pp. 4802–4807.
- [21] Carson, J. M., Açikmeşe, B., Murray, R. M., and MacMynowski, D. G., “A Robust Model Predictive Control Algorithm with a Reactive Safety Mode,” *IFAC World Congress*, edited by M. J. Chung and P. Misra, Vol. 17, Gangnam-gu Seoul, South Korea, July 2008, pp. 13175–13181.
- [22] Lavalle, S., *Planning Algorithms*, Cambridge University Press, 2006.
- [23] Janson, L., Schmerling, E., Clark, A., and Pavone, M., “Fast Marching Tree: A Fast Marching

- Sampling-Based Method for Optimal Motion Planning in Many Dimensions,” *International Journal of Robotics Research*, Vol. 34, No. 7, 2015, pp. 883–921.
- [24] Starek, J. A., Barbee, B. W., and Pavone, M., “A Sampling-Based Approach to Spacecraft Autonomous Maneuvering with Safety Specifications,” *AAS GN&C Conference*, Vol. 154 of *Advances in the Astronautical Sciences*, Breckenridge, CO, Feb. 2015, pp. 1–13.
- [25] Starek, J. A., Maher, G. D., Barbee, B. W., and Pavone, M., “Real-Time, Fuel-Optimal Spacecraft Motion Planning under Clohessy-Wiltshire-Hill Dynamics,” *IEEE Aerospace Conference*, Big Sky, MT, March 2016, pp. 1–15, Accepted.
- [26] Ross, I. M., “How to Find Minimum-Fuel Controllers,” *AIAA Conf. on Guidance, Navigation and Control*, Providence, RI, Aug. 2004, pp. 1–10.
- [27] Clohessy, W. H. and Wiltshire, R. S., “Terminal Guidance System for Satellite Rendezvous,” *AIAA Journal of the Aerospace Sciences*, Vol. 27, No. 9, Sept. 1960, pp. 653–658.
- [28] Hill, G. W., “Researches in the Lunar Theory,” *JSTOR American Journal of Mathematics*, Vol. 1, No. 1, 1878, pp. 5–26.
- [29] Bodson, M., “Evaluation of Optimization Methods for Control Allocation,” *AIAA Journal of Guidance, Control, and Dynamics*, Vol. 25, No. 4, July 2002, pp. 703–711.
- [30] Dettleff, G., “Plume Flow and Plume Impingement in Space Technology,” *Progress in Aerospace Sciences*, Vol. 28, No. 1, 1991, pp. 1–71.
- [31] Starek, J. A., Açıkmese, B., Nesnas, I. A. D., and Pavone, M., “Spacecraft Autonomy Challenges for Next Generation Space Missions,” *Advances in Control System Technology for Aerospace Applications*, edited by E. Feron, Vol. 460 of *Lecture Notes in Control and Information Sciences*, chap. 1, Springer, Sept. 2015, pp. 1–48.
- [32] Barbee, B. W., Carpenter, J. R., Heatwole, S., Markley, F. L., Moreau, M., Naasz, B. J., and Van Eepoel, J., “A Guidance and Navigation Strategy for Rendezvous and Proximity Operations with a Noncooperative Spacecraft in Geosynchronous Orbit,” *AIAA Journal of the Aerospace Sciences*, Vol. 58, No. 3, July 2011, pp. 389–408.
- [33] Schouwenaars, T., How, J. P., and Feron, E., “Decentralized Cooperative Trajectory Planning of Multiple Aircraft with Hard Safety Guarantees,” *AIAA Conf. on Guidance, Navigation and Control*, Providence, RI, Aug. 2004, pp. 1–14.
- [34] Fehse, W., *Automated Rendezvous and Docking of Spacecraft*, Vol. 16, Cambridge University Press, 2003.
- [35] Fraichard, T., “A Short Paper about Motion Safety,” *Proc. IEEE Conf. on Robotics and Automation*,

- Roma, Italy, April 2007, pp. 1140–1145.
- [36] Alfriend, K., Vadali, S. R., Gurfil, P., How, J., and Breger, L., *Spacecraft Formation Flying: Dynamics, Control and Navigation*, Vol. 2, Butterworth-Heinemann, 2009.
- [37] LaValle, S. M., *Planning Algorithms*, Cambridge University Press, 2006.
- [38] Janson, L., Ichter, B., and Pavone, M., “Deterministic Sampling-Based Motion Planning: Optimality, Complexity, and Performance,” *International Symposium on Robotics Research*, Sestri Levante, Italy, Sept. 2015, In Press.
- [39] Halton, J. H., “On the Efficiency of Certain Quasirandom Sequences of Points in Evaluating Multidimensional Integrals,” *Numerische Mathematik*, Vol. 2, 1960, pp. 84–90.
- [40] Allen, R. and Pavone, M., “A Real-Time Framework for Kinodynamic Planning with Application to Quadrotor Obstacle Avoidance,” *AIAA Conf. on Guidance, Navigation and Control*, San Diego, CA, Jan. 2016, Submitted.
- [41] Schmerling, E., Janson, L., and Pavone, M., “Optimal Sampling-Based Motion Planning under Differential Constraints: the Drift Case with Linear Affine Dynamics,” *Proc. IEEE Conf. on Decision and Control*, 2015, In Press.
- [42] Schmerling, E., Janson, L., and Pavone, M., “Optimal Sampling-Based Motion Planning under Differential Constraints: the Driftless Case,” *Proc. IEEE Conf. on Robotics and Automation*, 2015, pp. 2368–2375.
- [43] *Close proximity* in this context implies that any higher-order terms of the linearized relative dynamics are negligible, *e.g.*, within a few percent of the target orbit mean radius.
- [44] Goward, S. N., Masek, J. G., Williams, D. L., Irons, J. R., and Thompson, R. J., “The Landsat 7 Mission: Terrestrial Research and Applications for the 21st Century,” *Remote Sensing of Environment*, Vol. 78, No. 1–2, 2001, pp. 3–12.
- [45] All simulations were implemented in MATLAB 2012b and run on a Windows-operated PC, clocked at 4.00 GHz and equipped with 32.0 GB of RAM. CVXGEN and CVX [46], disciplined convex programming solvers, were used to implement Δv allocation and trajectory smoothing, respectively.
- [46] Grant, M. and Boyd, S., “CVX: Matlab Software for Disciplined Convex Programming, Version 2.1,” <http://cvxr.com/cvx>, June 2015.